AN ANALYSIS OF MULTISPECTRAL UNMANNED AERIAL SYSTEMS FOR SALT MARSH FORESHORE LAND COVER CLASSIFICATION AND DIGITAL ELEVATION MODEL GENERATION

by

Logan D. Horrocks

A thesis submitted in fulfillment of the
requirements of GEOG 4526

for the Degree of Bachelor of Science (Honours)

Department of Geography and Environmental Studies
Saint Mary's University
Halifax, Nova Scotia, Canada

April 11th, 2018

Members of the Examining Committee:

Dr. Danika van Proosdij (Supervisor)
Department of Geography and Environmental Studies,
Saint Mary's University

Dr. Philip Giles
Department of Geography and Environmental Studies
Saint Mary's University

ABSTRACT

An Analysis of Multispectral Unmanned Aerial Systems for Saltmarsh Foreshore Land Cover Classification and Digital Elevation Model Generation

by

Logan D. Horrocks

Recent advances in Unmanned Aerial Systems (UAS), and increased affordability, have proliferated their use in the scientific community. Despite these innovations, UAS attempts to map a site's true elevation using Structure from Motion Multi-View Stereo (SFM-MVS) software are obstructed by vegetative canopies, resulting in the production of a Digital Surface Model (DSM), rather than the desired Digital Elevation Model (DEM). This project seeks to account for the varying heights of vegetation communities within the Masstown East saltmarsh, producing DEMs for mudflat/saltmarsh landscapes with an accuracy comparable to that the DSM. DEM generation has been completed in two separate stages. The first stage consists of land cover classifications using UAS derived, radiometrically corrected data. Respective land cover classifications are assessed using confusion matrices. Secondly, surveyed canopy heights and function derived heights are subtracted from their respective classes, generating the DEMs. DEM validation has been performed by comparing topographic survey point values to those modeled, using the Root Square Mean Error (RMSE) measure. The project then compares the various parameters implemented for land cover classifications, and DEM accuracy. DEM generation methods were then coupled to produce a final DEM with a RMSE of 6cm. The results suggest consumer grade Multispectral UAS can produce DEMs with accuracies comparable to the initial DSMs generated, and thus merit further studies investigating their scientific capacities.

April 11th, 2018

RÉSUMÉ

Une analyse des systèmes aériens multispectraux téléguidés pour la classification de la couverture terrestre et la génération numérique de modèles d'élévation dans le cas de marais estuariens

Par Logan D. Horrocks

Les progrès récents dans les systèmes aériens téléguidés (UAS) et leur accessibilité croissance ont favorisé leur utilisation au sein de la communauté scientifique. Malgré ces innovations, les UAS tentent de cartographier l'élévation de la surface d'un site obstrué par la végétation à partir du logiciel « Motion Multi-View Stereo » (SFM-MVS); aboutissant à la création d'un Modèle Numérique d'Élévation (MNE) au lieu du Modèle Numérique de Terrain (MNT) souhaité. Ce projet vise à quantifier les différentes hauteurs des communautés végétales dans le marais salé de Masstown Est, en produisant des MNE pour les paysages de marais/vasières avec une précision comparable à celle des MNE. La génération des MNT a été réalisée à partir de deux étapes distinctes. La première étape repose sur des classifications de la couverture terrestre à partir de données UAS dérivées, corrigées radiométriquement et géométriquement. Les classifications de la couverture terrestre sont évaluées à partir de matrices de confusion. Dans un second temps, les hauteurs de la canopée étudiée et les hauteurs dérivées de la fonction sont soustraites de leurs classes respectives, générant les MNT. La validation des MNT a été réalisée en comparant les valeurs des relevés topographiques avec les valeurs modélisées, en utilisant la mesure de l'erreur quadratique moyenne (EQM). Le projet compare ensuite les différents paramètres mis en place pour les classifications de la couverture terrestre et la précision du MNT. Les méthodes de génération de MNT ont ensuite été couplées pour produire un MNT final avec une EQM de 6 cm. Les résultats indiquent que les UAS multispectraux « Grand public » peuvent produire des MNT avec des précisions comparables aux MNE initiaux générés, et mériteraient ainsi d'autres études quant à leur valeur scientifique.

Le 11 Avril, 2018

ACKNOWLEDGEMENTS

TABLE OF CONTENTS

LIST OF TABLES

LIST OF FIGURES

CHAPTER 1

Introduction and Literature Review

1.1. Introduction

Recent advances and increased affordability in Unmanned Aircraft Systems (UAS) technology have rendered their use widespread in the scientific community (Colomina and Molina, 2014; Crutsinger *et al*., 2016). UAS are comprised of Unmanned Aerial Vehicles (UAVs), the respective controller system, and the communication system which connects the two (ICAO, 2011). UAS have been used for numerous applications and disciplines ranging from agriculture (Horton *et al*., 2017; Wu *et al*., 2017), forestry (Hogan *et al*, 2017), land degradation, (Yengoh et al., 2015) and conservation (Husson et al., 2017).

The products generated from remote sensing systems are largely limited by vegetation cover when trying to acquire true landform elevations for Digital Elevation Models (DEMs), creating Digital Surface Models (DSMs) instead (Carrivick *et al*, 2016). DEMs of a suitable accuracy may be used for numerous geomorphic, landform, and hydrographic analyses (Gonçalves & Henriques, 2015; Jaud et al., 2016). DEMs captured over a successive timespan may reveal further change within a landscape (Lucieer & Jong, 2014; Haas et al., 2016). Those who employ remote sensing techniques are faced with the availability of ever-increasing precision and accuracy of their instruments, coupled with the emergence of new innovations (Crutsinger *et al*., 2016). Having examined the tool kits, practices and classifications of others with larger UAS craft and more refined sensors, it has been suggested that consumer grade multispectral sensors merit investigation on their capacity to classify saltmarsh covers and

produce DEMs (Harwin and Lucieer, 2012; Jaud *et al*., 2016; Long *et al*., 2016; Kalacska *et al*., 2017). Means of incorporating variables beyond reflectance values (such as elevation) in multivariate classifications also supported the idea that surface cover delineation could be successfully performed with a high degree of accuracy (Grebby *et al*., 2010).

This research will determine what combination of parameters for a multispectral equipped UAS will yield the most accurate and useful land cover classifications and DEM for the saltmarsh landscape. These parameters include flight altitudes of 50, 70, and 90 meters, classification schemes with different five and six landcover classes, and two canopy adjustment methods for the present species of vegetation. The objective of this project is to produce a DEM with a tolerable accuracy through generating the suite of geospatial products required. An ideal accuracy for the DEM would rival the accuracy of the DSM in areas if bare surface (lacking vegetative cover).

This study employed DJI Phantom 3 Drone modified to carry a Parrot Sequoia Multispectral Sensor to classify surface covers in the Masstown East Saltmarsh. Following the classifications of surface covers in the site with kappa coefficients greater than 0.8, the study seeks to derive DEMs from DSMs for the site by accounting for varying heights of vegetative communities. The derivation of DEMs with classified covers has been completed with two separate methods representing canopy height(s). Further analysis exploring supervised classifications, DEM generation, and their errors has been performed to quantitatively assess the potential of UAS mounted multispectral sensors. The results from this project may then serve as guidelines or recommendations regarding project and flight set up for future studies seeking to employ UAS for scientific research.

1.2. Literature Review

This literature review will commence its investigation with an overview of remote sensing, examining the various impacts of resolution, and the different classification processes. The development of the Structure from Motion Multi-View Stereo (SfM-MVS) processing and multispectral sensors for UAS will then be investigated. The review considers the components of a saltmarsh, followed by investigation of feedbacks within the system using concept of Ecogeomorphology. Finally, the application of remote sensing systems for mapping saltmarshes will be examined, illustrating the variety of disciplines that may benefit from the geospatial products.

1.2.1. Remote Sensing Overview

1.2.1.1. Recent History and Application

In the last twenty years, there have been tremendous developments within the field of remote sensing of vegetation (Crutsinger, 2016; Aguilera and González, 2017). High resolution imagery from various sources has reached the most accessible levels in history in terms of price and availability (Colomina and Molina, 2014), furthering the demand for high quality end products from a multitude of fields and across various sectors. Among the many uses of remotely sensed data, the identification and monitoring of land covers and vegetative species remains a key component for practices such as conservation and restoration (Peacock, 2014; Whitehead and Hugenholtz, 2015). The ability to produce secondary products such as DSMs and DEMs is also of high importance for numerous other applications such as the production of slope maps, average insolation and windspeed maps, used in a variety of other domains (Carrivick *et al.*,

2016). The ability to produce DEMs of a suitable accuracy for further analysis is a function of the levels of resolution of the sensor and platform in use.

1.2.1.2. Resolution

When acquiring remotely sensed data, there are a few primary considerations which will guide the entire acquisition process: the purpose of the data, the subject being studied, and the context. One must have a clear purpose in their pursuit to generate a useful end-product that properly addresses the fundamental research question. Once addressed, one can start to determine the resolution needed to observe the desires phenomena. For this to be accomplished, there must be a solid understanding of the components that make up resolution. Four types of resolution exist and allow users to determine the suitability of a set of imagery for their selected purpose; *spatial, spectral, radiometric and temporal* (Fox III, 2015).

Spatial resolution refers to the size of ground resolution cell (area on the earth), represented by each pixel in the image. The term ground sample distance (G.S.D) refers to the distance on earth between the midpoints of pixels. Small objects can be identified in high or fine spatial resolution (NRCAN, 2013). Following the example in Figure 1.1, there are more pixels
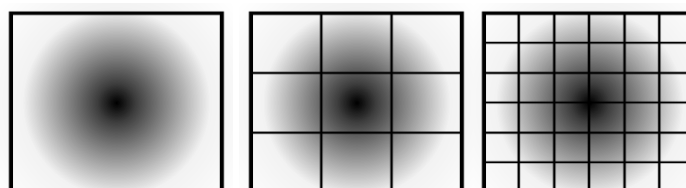
Figure 1.1: Spatial Resolution Example. Reproduced from Giles, P. (2016).
Remote Sensing of the Environment, Class 6: Radiometric Resolution;
Atmospheric influences; Image enhancement.

making up a feature in a high spatial resolution image than a low-resolution image (Spring *et al*., 2016).

Radiometric resolution refers to the relative widths of brightness intervals. These intervals can be visualized as the quantity of brightness steps utilized by the image, as shown in Figure 1.2. A higher radiometric resolution will have more steps than a low-resolution image, thus better representing the variation in brightness and rendering it more informative (Fox III, 2015). This can be directly observed in the brightness steps of Figure 1.2.

Spectral resolution describes the wavelength range of spectral bands that make up the image, with each band denoting a certain range of radiation the sensor is receptive to (Fox III, 2015). An image may be comprised of multiple bands, yet it is only possible to display three at a time due to the three color guns available (R,G,B) available for display on LCD monitors. Figure 1.3 displays various sets of sensors and their respective spectral resolutions.

Temporal resolution describes the frequency (timespan) between data collections the sensor and platform are capable of (Fox III, 2015). Depending on the platform in use, the return time between data collection can vary greatly. Multiple image sets are required to observe, measure, and compare changes in observed phenomena.

Bits	Value Range	Number of Brightness Levels
1Bit	$2^1 = 2$ (0-1)	0 [___] 1
4Bit	$2^4 = 16$ (0-15)	0 [___] 15
8Bit	$2^8 = 256$ (0-255)	0 [___] 255
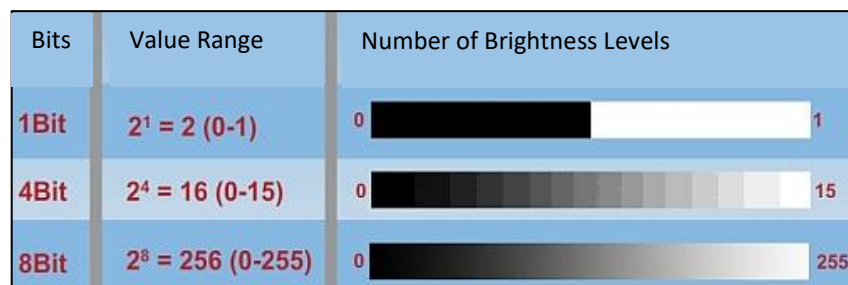
Figure 1.2: Radiometric Resolution Example. Reproduced from: Geographisches Institut der Universität Bonn. (n.d.). Radiometric Resolution. Retrieved from http://www.fis.unibonn.de/en/recherchetools/infobox/professionals/resolution/radiometric-resolution

Temporal resolution can range anywhere from a 15-minute interval (a drone flight and replacing batteries), to semi-annually, and potentially even infinitely depending on the platform. As seen on Table 1.1, there exists a range of temporal resolutions for various satellites. UAS offer new levels of temporal resolution; the term is increasingly irrelevant for UAS photogrammetry as flights can be performed as the user desires. A major benefit of UAS is that the timing and frequency of data collection is under the user's control. With an understanding of the four characteristics of resolution and the demands of one's project, one can start to evaluate the suitability of different sensors and the host platforms for their desired data (Fox III, 2015).
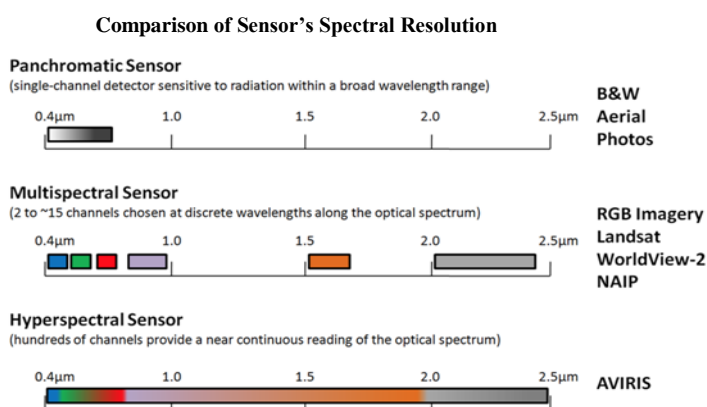
Figure 1.3: Spectral Resolution Example via Different Sensors. Reproduced from: Harris Geospatial. (2013). Figure 3: Spectral Resolution of Different Sensors

Comparison of Sensor's Temporal Resolution

Temporal resolution (d)	Spatial resolution[b] (m)	
	1-5	6-10
Daily 2-7	(QuickBird)[c] (ALOS AVNIR-2) (Orbview-3,4) (QuickBird) (SPOT-5a,b 3xHRVIR)	(Almaz-1b MSU-E2) (ALOS AVNIR-2) (ARIES-1) IRS-1C,D PAN (Orbview-4) SPOT-4 2xHRVIR (SPOT-5a,b 3xHRVIR)
8-15	Ikonos	IRS-1C,D PAN Priroda/Mir MOMS-2P
15-30		IRS-1C,D PAN SPOT-2 2xHRV
>30	(ALOS AVNIR-2)	(ALOS AVNIR-2)

Table 1.1: Temporal Resolution Examples via Satellite Return Period. Reproduced from: Obregon, R. (2009). Table 4: Current and proposed sensor systems for identifying and mapping urban features.

1.2.1.3. Pre-Processing: Calibrations

As recent advances in the remote sensing industry have led to widespread implementation and combination of technologies, it becomes increasingly important to objectively evaluate the products generated. Measures can be taken before and after the flight to achieve the highest quality of data; these processes are calibration, pre-processing, and post-processing (Kumar,

2012). The calibration process takes place before any flights, while both pre-processing and post-processing occurs after flights. Calibration ensures that the data collected are accurate and representational of the observed surface. Pre-processing includes rectification, restoration, and image enhancement, while post-processing concerns itself with information extraction (Kumar, 2012).

Calibration is employed to standardize the results gathered based on the specifics of the sensor, lens and platform in use. Calibrating a multispectral sensor radiometrically ensures that the radiance in the images are representative of true surface reflectance (Kumar, 2012), adjusting for uneven response across the sensor (Crisp, 2001). Targets with standardized reflectance values can be employed to calibrate the sensor, ensuring it portrays values as intended. Radiometric calibrations for illumination differences differ greatly for sensors and platforms in use. For satellites, little can be done in the way of accounting for solar exposure at that given site, while for UAS, sunlight sensors can be attached atop the platform to account for incoming radiation (Parrot, 2016). For example, the Parrot Sequoia utilizes a sunlight or 'irradiance' sensor to account for illumination and give absolute measurements (Parrot, 2016).

Geometrical calibration attempts to account for variations in spatial accuracy within an image as a result of lens distortion. The typical method for geometric calibration includes the generation of an image distortion map to see where and in what magnitude distortions are present (Berni *et al*., 2009). An image with uniform points distributed throughout is used as the control, an image is taken and then a distortion map is generated to show areas of stretch and squeeze (Berni *et al*., 2009).

1.2.1.4. Spectral Response Curves

Every material absorbs, reflects and emits radiations in unique regions of the electromagnetic spectrum as a function of its physical state and chemical composition (Avery and Berlin, 1992). The field of remote sensing relies heavily upon the phenomena of unique absorption to identify and monitor land covers. Remote sensors can plot a graph for each cover with the electromagnetic spectrum on the X axis, and respective reflectance on the Y axis. As observed in Figure 1.4, reflectance values for a surface can vary across the spectrum (e.g., conifers), where other surfaces may remain relatively consistent (e.g., water). By creating a spectral response curve for each surface, one can start to observe how each surface reflects and emits light uniquely. These spectral response curves are utilized in the creation of spectral signatures, which are then used to help classify imagery per land cover, acting as an input or set of rules to help the computer distinguish and recognize surfaces. With suitable spatial and spectral resolution, these signatures also have the potential of classifying different vegetation covers.
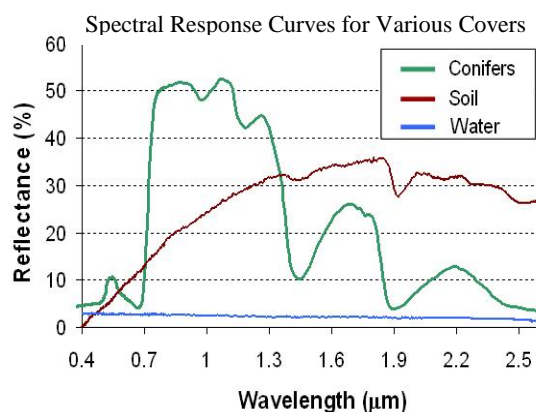
Figure 1.4: Spectral Response Curves, Reproduced from:
Eumetrain. (2010). Spectral signature of an object.

There exist many examples where the creation of spectral response curves has been performed with a high degree of success using high resolution satellite imagery taken with a hyperspectral sensor (Kokaly 2007, Berni *et al*., 2008; Grebby *et al*, 2010; Parent *et al*., 2015). There is also a growing trend in UAS based signature generation with the advancements of both sensor platform and technology (King *et al*., 2005; Berni *et al*., 2008; Whitehead and Hugenholtz, 2015; Heipke 2016; Aguilera and González, 2017). Hyperspectral sensors have traditionally been the popular choice for species level classifications due to the high spectral resolution; with narrower and more bands, it is easier to find some region in which the spectral reflectance properties of species may differ.

1.2.1.5.   Post Processing: Unsupervised and Supervised Classification

Post processing involves information extraction processes such as unsupervised and supervised classification. These processes automate identification of covers quantitatively (Kumar, 2012). Although some suggest this may replace visual analysis (Kumar, 2012), there exists limits to the accuracy and reliability of the technology (Crutsinger, 2016).

In remote sensing, image classification is generally grouped into two categories: unsupervised and supervised classification. Unsupervised Classification "investigates data statistics by subdividing the image into clusters of pixels with similar characteristics" (Li et al., p.1, 2015), most commonly through Iterative Self-Organizing Data Analysis (ISODATA) or K-mean classification (Li et al., 2015). On the other hand, "Supervised techniques are characterized by finding explicit relationships between samples and classes" (Li et al., 2015). Unsupervised classification typically requires less initial time input, but the output is of a different nature than a

supervised classification as there is no user defined training datasets (Peacock, 2014). Quality of the supervised classification is also found to have improved if the user has a previous understanding of the type of cover in the image (Jensen, 2005).

Signature generation is a process that comes about in the steps of supervised classification. Supervised classification works with the user specifying pixels that belong to a certain cover class, (e.g., water). Small polygons are constructed over the raster surface with a representative range of Digital Number (DN) values within the cover. These are the input training pixels the computer will use to generate the signatures used for the classification (Rumiser *et al*., 2013). Once a representative number of polygons have been constructed to show a representation of the variation within a class (comprising multiple signatures), a new signature that combines all is created to be representative of the entire class. For each class and thus each cover, the process is repeated to make a representative class signature. The class signatures are then saved as a signature set (Rumiser *et al*., 2013), and are ready for their first implementation.

The signature set is applied to the image data as the input signature file. Analysis of the classification can then be performed to determine the number of pixels in each class (Rumiser *et al*., 2013), and if any pixels were misclassified in the classification. Following the initial signature generation, the classification may be repeated with slight modifications to the input signatures depending on the results. Signatures would be modified by selecting additional training sites, to include representative pixels omitted (Rumiser *et al*., 2013). The signature set and the algorithm are selected to perform the classification. Different algorithms serve as different guiding rules which will be used to assign all pixel values in the image to a class. This project has selected the Maximum Likelihood Algorithm.

One of the essential steps required in the remote sensing process is ground truthing. Ground truthing is the selection of ground resolution cells with known cover characteristics as training sites (NRCAN, 2013). By selecting a plot with known vegetation covers, one can be certain that the output signatures are as accurate as possible (Rumiser *et al*., 2013). There is no set number of training pixels 'required' for a supervised classification, however studies often employ $10n$-$100n$ pixels per class, where n is the number of bands input into the classification (Jensen, 2005). In selecting these pixels, one attempts to select as many sites as required to represent the entire range of DN values within the cover. Assessments of the sizes and distribution of plant communities should be considered before any flight as the spatial resolution of the imagery must be finer than the phenomena that is to be observed.

1.2.1.6.   Classification Algorithms and Accuracy Assessments

As different algorithms exist to assign unknown pixels to a class, it becomes increasingly important to understand the logic and the assumptions upon which the algorithms operate. The algorithm used in this process is the Maximum Likelihood classification. Figure 1.5 graphically displays how this algorithm operates. Maximum Likelihood assigns unknown pixels to a class by computing the standard deviations from the multivariate mean for each class and placing pixels in their most probable class (Kumar, 2012). This algorithm assumes that each class has a normal distribution in each band. If the data displays a bi-modal or tri-modal distribution, it is likely the modes should be separate classes (Kumar, 2012). This method of classification is considered to be the most statistically accurate, and the most computationally demanding (Peacock, 2014).
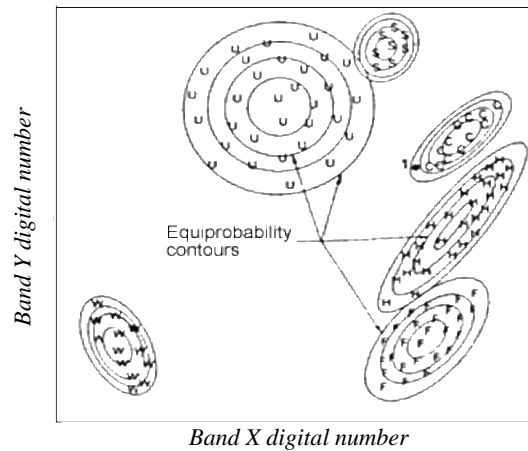
Figure 1.5: Maximum Likelihood Classifier.
Reproduced from: Lillesand, T. M., and Kiefer, R. W.
(1987). Remote sensing and image interpretation
(2nd ed.). New York: J. Wiley (Fig b).

1.2.2. SfM-MVS and UAS Development

1.2.2.1.   History/Application SFM MVS

This section will briefly introduce and explore the developments of both SfM-MVS and

UAS technologies. Recent studies successfully employing both UAS and SfM-MVS in varying

degrees will then be examined.

Structure from Motion Multi-View Stereo (SfM-MVS) is a two-part method of generating

3-D models from 2-D images (Westoby et al, 2012). The method has undergone numerous

developments and innovations since its debut in the 1980s, largely due to advancements in

software and graphical user interfaces (Carrivick *et al*., 2016). SfM employs algorithms to

identify matching or common pixels in overlapping sets of imagery, calculating the orientation

and location of the camera from the differential position of common pixels (Carrivick *et al*.,

2016). These calculations are then utilized to create a 3D point cloud model of the scene from the

various overlapping 2D images. The initial sparse point cloud is densified and rendered to a finer

resolution, or 'Dense Point Cloud' with MVS methods. Carrivick *et al*. (2016) emphasize that SFM-MVS methods are still in their infancy, requiring more research and analysis of accuracy to reach their true potential in the geosciences.

1.2.2.2 Development of UAS Platforms and Respective Sensors

The term UAV has been deemed obsolete by the International Civil Aviation Organization (2011), yet it is still appearing in much of the academic literature published of late (Long *et al*., 2016; Crutsinger *et al*., 2016). Advancements in sensor and platform technologies have resulted in the widespread deployment of UASs for multiple purposes, including data acquisition. As explored by various authors including Colomina and Molina (2014) and Fox III, (2015), these sensors and platforms are continually becoming less expensive, while delivering finer and higher resolution data. There has been growing demand for the application and utilization of UAS technology within the academic community, as more academics learn what sorts of projects and data acquisition these technologies can perform for them. One of the greatest advancements this may yield is a shift towards "Remote Sampling" for many disciplines (UK Marine, 2001). This trend is partially due to the fact UAS technology can acquire high resolution data without disturbing or negatively impacting the landscape under observation when physically taking samples from it, or reducing the total area required to physically visit. As the associated sensor technology increases in terms of both spectral and spatial resolution, so will further demand for UAS based observation.

1.2.2.3. Applied UAS Studies: Multivariate Classifications and Accuracy Assessments

Yengoh *et al.* (2015) explore the ways in which the NDVI (Normalized Difference Vegetation Index) can be incorporated in generation of spectral signatures for monitoring land degradation, agricultural and ecosystem resilience, and desertification. Combined with other indexes (such as the Normalized Difference Water Index, NDWI), trained analysts can utilize NDVI further monitor drought, land productivity, carbon stocks, and habitat fragmentation (Yengoh *et al*, 2015; Stow *et al*, 2007). Other have sought higher spatial and spectral resolution data for precision application, such as Viticulture. Satesteban (2016) incorporated thermal imagery retrieved from a UAS to generate a crop water stress index (CWSI) representative of the site. Signatures can also be created using additional variables if they are in the exact same raster format; this process is called multivariate classification (Roe, 2006). Integrating the multispectral rasters with both NDVI and elevation data can yield a more accurate classification (Sturari *et al*., 2017). A study done by Grebby *et al*., (2010), attempted this, and generated lithological maps using the relationship between plants and topography. They found upon incorporating elevation data that they were about to improve their kappa coefficient from 65.5 to 88%. Furthermore, thermal imagery and the Normalized Difference indexes it can generate can be incorporated into the multivariate classification for an even more detailed product (Berni *et al*., 2008). Although additional variable inputs for a multivariate classification can produce more accurate and detailed products, there remains sets of assumptions and limits for every product.

1.2.3. Saltmarsh Landscape, Form and Ecogeomorphology

1.2.3.1. Macrotidal creek form and zonation of vegetation

This section will provide a review of the components that make up the dynamic system of the saltmarsh landscape and their interactions. Fagherazzi *et al.* (2002) describe the saltmarsh as a system in which the feedback between biota and landscape is extremely strong. They state that this relationship is strong enough to play a role in how these landscapes evolve, as well as their fate (Fagherazzi *et al.*, 2002).

Thus, to understand the landscape and its morphology requires an understanding of the biota, and vice versa. The Masstown Saltmarsh may be described as a finger marsh; a long marsh existing along a tidal channel (UMaine, 2017). Saltmarsh landscapes have been categorized by Amos (1995) into three main zones: the subtidal zone, the intertidal zone and the supratidal zone. As their names suggest, the subtidal zone occurs below the low water mark, while the supratidal zone occurs above the high tide mark. The intertidal zone is located between the other two, the high and low marks water respectively (Amos, 1995). The intertidal zone can be divided into three main zones: Tidal Flat/ Channel, Low Marsh and High Marsh (UMaine, 2017). Within the intertidal zone there exist a common zonation of vegetation. As noted by Fagherazzi *et al*. (2004), the zonation of vegetation species within the saltmarsh is a function of hydroperiod and salinity, and thus elevation and distance from tidal creeks also plays a role in determining what species will grow in a given location. For the case of the majority of salt marshes within the Minas basin, the low marsh is dominated by *Spartina alterniflora*; a marsh grass that thrives in the saline conditions and diurnal inundation (Allen, 2000). The high marsh is host to a larger diversity of

species with various salt tolerances but is generally dominated by *Spartina patens* and *Juncus geradii* (UMaine, 2017).

1.2.3.2. Ecogeomorphology: the Saltmarsh Landscape

The dynamic nature of the saltmarsh giving rise to its form and function is better understood through the concept of Ecogeomorphology. The discipline is defined as "the study of the coupled evolution of geomorphological and ecosystem structures" Fagherazzi, (2004, p. vii).

As a dynamic system, a saltmarsh with the proper conditions can keep pace with sea level rise (Throne *et al*., 2013). This process requires adequate accretion, either by minerogenic, surface deposition, or organogenic, subsurface accumulation (Allen, 1990), or a combination of the two. Saltmarsh vegetation such as *Spartina alterniflora* and *Spartina patens* exert a source of friction on the flowing tide, reducing flow velocity and wave action (Lightbody and Nepf, 2006). Pending an adequate reduction in velocity, the suspended particles in the water column can settle on the marsh surface (Lightbody and Nepf, 2006). The same vegetative covers account for subsurface accretion, through an accumulation of organic matter as rhizomatic root mats undergo their life cycles (Allen, 1990). Vegetative covers contribute to the composition of the marsh; Rinaldo *et al*., (2004) found interactions between the patterns in vegetation and the morphology of the marsh surface are key components of the landscape's dynamics. As tidal platforms accrete to elevation levels conducive of colonization by halophytic species (e.g., *Spartina alterniflora*), the network reaches a form of dynamic equilibrium and experiences only minor alterations afterwards (Rinaldo *et al*., 2004.)

1.2.4. Application of Remote Sensing in Saltmarshes

1.2.4.1. Application of UAS and Remote Sensing in Saltmarshes

This section will investigate the various projects within saltmarsh ecosystems that have employed UAS technology. These projects can be divided into two broad classes: orthomosaics and elevation models. As reviewed in previous sections, SFM -MVS and UAS technologies have undergone significant advancements in the past five years (Crutsinger, 2016; Aguilera and González, 2017; Carrivick *et al*., 2016). This has allowed some to claim that SFM-MVS will 'revolutionize' analysis of tidal systems (Kalacska *et al*., 2017). Numerous projects utilizing UAS and SFM-MVS have reported elevation error values ranging from 1.5cm - 10cm (Harwin and Lucieer, 2012; Jaud *et al*., 2016; Long *et al*., 2016; Kalacska *et al*., 2017) within saltmarsh landscapes, with sensors ranging from Red, Green Blue (RGB); Multispectral; and Light Detection and Ranging (LIDAR) capabilities.

When comparing the DSMs of saltmarshes derived from LiDAR and SFM-MVS to DGPS surveyed elevations, Kalacska *et al*. (2017) found UAS average elevation error in the range of 2.1-3.6 cm, and 13-29 cm for LiDAR respectively. They claim LiDAR coverage, although quicker that SFM-MVS and DGPS surveys and less intrusive, does not provide the required resolutions required to analyze features of interest (Kalacska *et al*., 2017).

Notably, Medeiros *et al*. (2015) and Hladik and Alber (2012) attempted to produce valid DEMs representative of the tidal flats elevation by accounting for the varying heights and biomass of vegetation species. Medeiros *et al*., (2015) employed a methodology that examined the relation between biomass measurements to remotely sensed data for each class and created species independent LiDAR DSM adjustment values to more accurately determine tidal platform

elevation. RMSE of the LiDAR derived DEM was improved from 0.65m to 0.40m when incorporating the adjustment values (Medeiros *et al*., 2015).

Recent development in the field of remote sensing describes the new possibilities emerging for both researchers and practitioners (Colomina and Molina, 2014). Remote sensing researchers are faced with an ever-increasing precision and accuracy of their instruments, coupled with the emergence of new ones (Crutsinger *et al*., 2016). The examination of the tool kits and practices of others suggest that multispectral imagery is effective for generation of monoculture specific spectral signatures and image classification. Means of incorporating variables beyond multispectral imagery (such as elevation) in a multivariate classification also supports the idea that species identification can be successfully performed (Grebby *et al*., 2010). Further research attempting supervised classification, comparing outputs and their errors, needs to be performed to quantitatively asses the suitability and accuracy of UAS mounted multispectral sensors for vegetation species identification.

1.2.4.2. The Anthropogenic and Ecological Importance of Saltmarshes

As complex and diverse ecosystems, saltmarshes provide food and habitat to a vast range of species. Saltmarshes provide humans with countless benefits, quantified as ecosystem services (Biodiversity Information System for Europe, 2010). These services range in their nature and output, yet many aspects of our culture and economy are dependent upon them (JCU, 1995; Sousa *et al*., 2016). Their ecological importance and our dependence on these systems has led many to call for their conservation and continued monitoring (Chmura, 2013; Hopkinson et al., 2012; Deegan *et al*., 2012; Beaumont *et al*., 2013).

Saltmarshes have been found to be tremendous sequesters of carbon (Macreadie 2014; Beaumont *et al*., 2013). The plant communities within the marsh, largely *Spartina alterniflora* and *Spartina patens,* perform photosynthesis and convert $C0_2$ in the atmosphere into sugars, which are stored in their root masses. As these undergo cycles of thriving and perishing, carbon is accumulated below ground (Allen, 1990). It is estimated that saltmarshes sequester 4.6 – 8.7 teragrams of carbon dioxide annually (Quintana-Alcantara and Eduardo, 2014). The system is important for other nutrient cycles, including that of nitrogen and potassium (Sousa *et al*., 2010). The saltmarsh is also the habitat of many vegetative, invertebrate, fish, and bird species (Wiegert *et al*., 1981). Atlantic Canadian saltmarshes are home to rare and endangered species including the piping plover (Environment Canada, 2012) and Eastern Lilaeopsis and Eastern Baccharis (GOC, 2017).

The saltmarsh provides a valuable coastal barrier for any feature immediately upland of the marsh (Pendle, 2013). Not only does the saltmarsh thrive on regular tidal inundations, but the vegetation within the marsh dissipates oncoming wave energy (Lightbody and Nepf, 2006). Moreover, saltmarshes are increasingly valuable when they are in front of a dyke feature, as they can greatly reduce maintenance costs associated with waves and storms (Gedan et al., 2011; Pendle, 2013).

CHAPTER 2

Study Area: Masstown East

2.1. Masstown East Overview

The area of study is the eastern portion of the Masstown Saltmarsh, located in the Minas Basin, Nova Scotia. The Minas Basin is in the upper reach of the Bay of Fundy as seen in Figure 2.1. It is a macrotidal system, possessing a tidal range of 16m at its peak (NOAA, 2017). The site has high concentrations of suspended sediment, with maximums in the range of 6 g/l (G. Matheson, personal communication, August 2017). The marsh is minerogenic, with organic matter contents ranging from 0.5% - 4 % respectively (Matheson, personal communication, August 2017). The site has experienced a historic trend of progradation (Matheson, personal communication, March 2018), as well as having been dyked and being historically managed this way (Landscape of Grand Pre, 2017). Within the marsh, the practice of digging borrow pits has been employed to provide material to top the dykes, keeping the agricultural land behind the structure from flooding. This practice requires excavating channels in the marsh, or 'pits' as a source of material for dyke topping (Bleakney, 2004). The borrow pits within the Masstown East saltmarsh have demonstrated trends of infill of 10-15 cm/year over the past year (Matheson, personal communication, March 2018), and being colonized by the low marsh species *Spartina alterniflora.* The borrow pit and dyke features result in cross sectional elevation profiles that are atypical relative to non-modified marsh platforms.

The study site contains the remnants of a historic dyke feature running through the middle of the platform, east to west. The dyke was abandoned when the current one was built further behind it (Matheson, personal communication, March 2018). This has resulted in a greater accommodation space for the marsh. The area of study is approximately 12.5 acres.
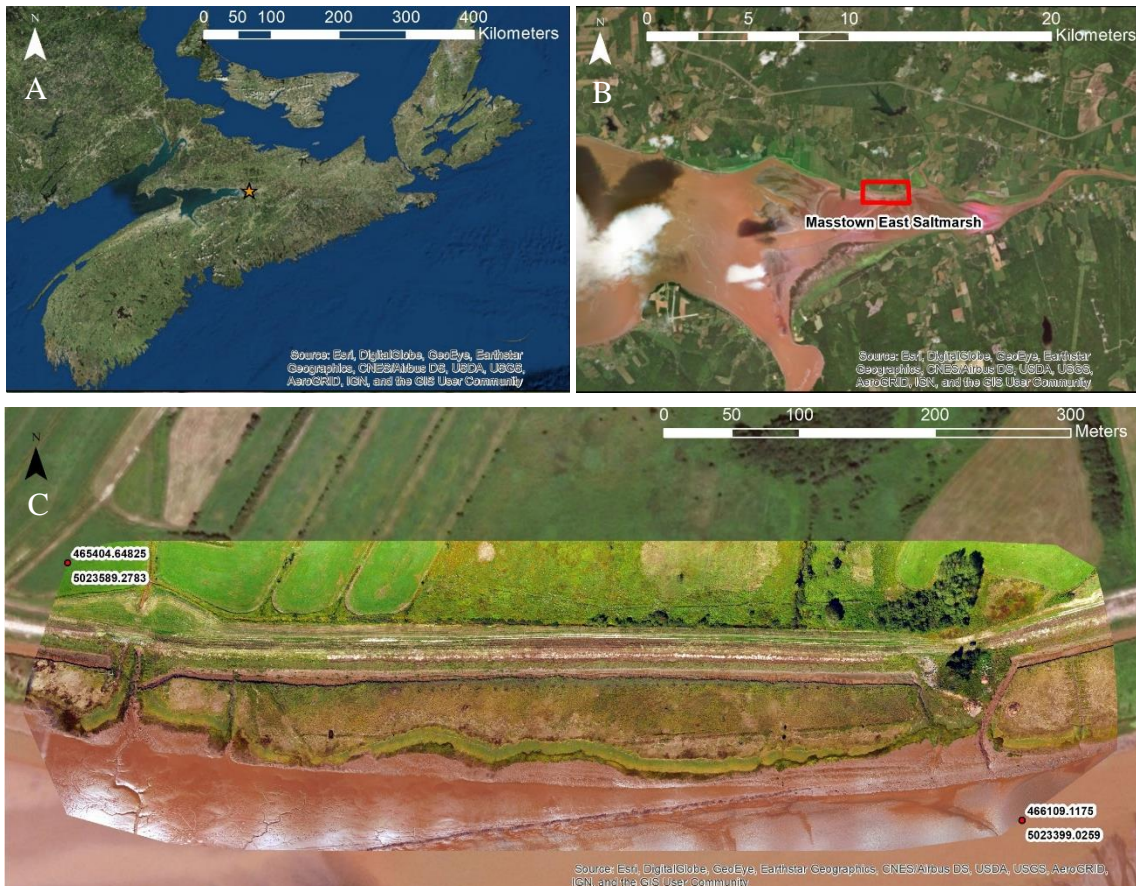
Figure 2.1 (A-C): Study Site, Masstown East Salt Marsh. Maps showing study area of Masstown East and where it is situated in the province.

2.2. Masstown East Vegetation

The vegetation found at the site is a typical assortment of species seen in saltmarshes in the Bay of Fundy, and many of the Atlantic Provinces (Roberts and Robertson, 1986). The low marsh is dominated by *Spartina alterniflora*, while the high marsh is far more diverse. The high

marsh at the site is covered predominately in *Spartina patens* and *Juncus Geradii*. Other species within this zone include *Solidago sempervirens* (Seaside goldenrod), *Limonium vulgare* (Seaside Lavender), *Triglochin maritima* (Arrowgrass), *Glaux maritima* (Sea Milkwart), and *Spartina pectinata*.

The distribution and assortment of vegetation is visibly distinguishable in RGB imagery, appearing as bands parallel to the thalweg and running East-West in the site. The first band adjacent to the channel is the *Spartina alterniflora* monoculture, while the next higher band above it is largely *Spartina patens* with some *Spartina alterniflora* and *Trilochin maritima*. The last and uppermost zone is the High Marsh mix, largely consisting of patched of healthy and dead *Juncus geradii*, and small mixes of the mentioned high marsh species.

Figure 2.2: Saltmarsh zones of vegetation. Low to high marsh transition, low marsh in foreground, high marsh in background. Reproduced from: Zottoli, R. (2015, April 14). Spartina patens (Zone 3).

CHAPTER 3

Methodology and Data

3.0. Project Methodology

While the field of UAS remote sensing and SFM-MVS are still in their infancy, there lacks the extensive body of research on methods and accuracy that exists for satellite platforms. This project couples both methodologies previously tested in UAS applications with those inspired by methods used for other platforms and sensors. Methods and sequences in this project have been adopted from previous work and the respective findings, when possible. For example, G.C.P. orientation and deployment has been optimized from previous Maritime Provinces Spatial Analysis Research Center (Mp_Sparc) UAS flights and their outputs. The remaining sequences (such as orientation and deployment of training/testing polygons) were informed by the academic body of knowledge on the specific subject (e.g. training pixels for UAS derived data), and the broader subject (e.g. training pixels for data derived from all platforms) where additional information is required. The rigor of the sample set up was constrained by the time and funds available for the project and seeks to maximize product accuracy. The project consists of three core aspects: field work and ground truthing, Pix4D processing, and ArcGIS processing.

3.1. Field Work and Ground Truthing

A segment of the marsh spanning an area feasible to cover by foot was selected for the study site, spanning about 600m by 50- 90m. The segment of marsh was then divided into three cells labeled A, B and C, about 200m each in length as shown in Figure 3.1. The sample set of

one training polygon (2x2m) for each vegetated cover in each cell was then configured. The

potential locations for polygons were determined using freely available satellite imagery of the

site on Google Earth. Points with these locations for each polygon were then input into a Garmin

handheld GPS unit for the field (+/- 5m).

Vegetation survey quadrats of 0.5m by 0.5m were constructed and strung. Each quadrat

was divided into a 5x5 square grid, with 25 squares measuring 10x10cm each. This area

corresponds roughly to the G.S.D. of the Parrot Sequoia when flown at an altitude of 90m.

Polygon measuring ropes to deploy training polygons were crafted using 8m segments of

nylon rope with the ends tied together. The rope was marked at a one-meter interval with flagging
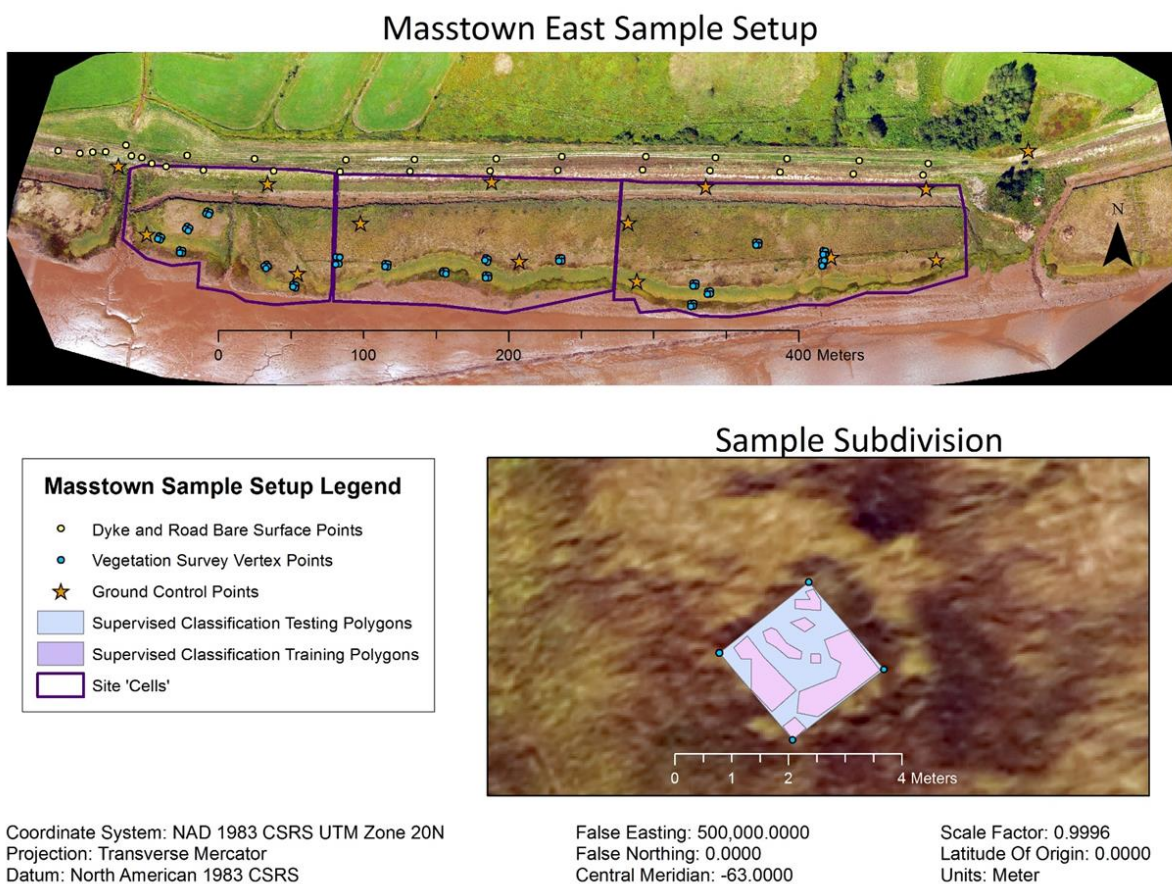
Figure 3.1: Site Sample Setup

tap to allow square and rapid deployment of the polygon. In the field, dowels were used to deploy the polygon. Following the vegetation survey, the dowels were replaced with flags for the topographic survey. The rope was then removed and used to guide the next training polygon. This method ensured all polygons were of a comparable area and geometry.

The vegetation surveys were performed three times in each polygon to validate the certainty of cover in the area. The locations of the vegetation survey with the polygon were chosen by a Random Number Generator (RNG) between 1-16. Each polygon of 2x2m can be divided into a grid of 4x4 with 16 cells measuring 0.5m by 0.5m each. These configurations were chosen as vegetation surveys require a minimum of 15% of an area to be surveyed to quantify covers within (USGS/NPS, 1994). As each of the three quadrats was 0.25 m^2, roughly 19% of each $4m^2$ training polygon was sampled. Tables and images from the vegetation survey are included in the appendix

The orientation of G.C.P.s attempts to minimize the number of G.C.P.s deployed, while spacing them appropriately through the study site. A minimum spacing of G.C.P.s is calculated as 1.5 times the smallest image dimension (Mpsparc, 2017). This calculated spacing ensures there is an adequate number of G.C.P.s visible in each image. As this project flew at various altitudes, the lowest altitude image dimensions were used for the G.C.P. spacing calculation. G.S.D. is the term used by the Pix4D program to describe the GRC of a given project. The G.S.D. of the UAS at 50m was 6.2cm, while the smallest dimension of image is 960 pixels. The product of the G.S.D. and pixels was multiplied by 1.5 to suggest a spacing of 90m.Therefore, G.C.P.s were not spaced more than 90m from the edge of the study site, or each other. This ensures that there is minimal warping and distortion within the DSM of the study site.

G.C.P.s were deployed on September 14th, and the UAS flights completed between the 14th and the 15th. The flights were completed with a 85% frontlap and a 70% sidelap between images, nadir, and at altitudes of 50, 70, and 90m respectively. All G.C.P.S, polygon vertices, and vegetation survey locations were surveyed using the Leica GS-14 GNSS RTK Rover, with sub-centimeter horizontal and vertical accuracies.

Vegetation surveys included a list of species, hits (where species intersects with the survey grid), percent cover, plant height (height of the entire plant), and canopy height (the height at which the plant stands). Canopy height and plant height may be identical or may vary greatly if the plant 'lays' on the ground. An image was taken with a GPS camera at the location of each survey. The images include the plot, the quadrat, and a labeled whiteboard detailing the survey number. Percent cover was estimated based on visual observation, while all other measurements were collected quantitatively. Canopy heights were measured with a metal rod that had an adjustable and locking perpendicular piece (the arm). The rod was planted vertically in the ground and the arm locked at a height estimated to be representative of the mean canopy height. The rod was gently rotated, and the arm adjusted to intersect the maximum amount of canopy tops within its radius. The arm's final height above the surface is the mean canopy height for the area.

3.2. Pix4D Processing

The images collected from the various flights were uploaded into Pix4D mapping software, where initial point clouds are generated. The point clouds are then georeferenced with DGPS coordinates for each G.C.P. visible in the imagery set. The projected error for these

coordinates are also input into this process. For multispectral imagery sets, images taken prior to each flight of an Airnov calibration target (with known reflectance values) were used to radiometrically correct the Sequoia image and sunshine sensors. The processing parameters for the project are then set and run, generating the dense point cloud. From this point cloud, the DSM, orthomosaics and reflectance maps were generated and exported.

3.3. ArcGIS Processing

The data was amalgamated into an ArcGIS database. All data were input in the NAD 83 CSRS Zone 20N horizontal coordinate system and the CGVD 2013 vertical datum. Once all reflectance maps were input, indices were generated. For this project, an NDVI raster was generated from the NIR and Red reflectance maps at the varying altitudes. The project also generated and utilized the Normalized Difference Red Edge (NDRE) index (Spiral Commercial Services, 2015; MicaSense, 2017), using the NIR and Red Edge reflectance maps.

Following the generation of the indices, polygon and vegetation survey points were plotted. Polygons were created for each class by joining the surveyed vertices. Within these polygons, several iterations of random points were generated, with spacing corresponding to the G.S.D. Approximately 200 training and testing points were generated within each of the polygons. An intersection was then performed and all testing pixels within 13.3cm of a training pixel were deleted, ensuring no training or testing pixels exist in the same location and reducing the count below 200. The points served to break up the surveyed region into fragments, one set of shapefiles for testing pixels, and one set for training pixels. Shapefiles of training and testing pixels were also created using the pixels for each cover within Cells A and B, and Cell C.

Supervised classifications of the different flights were then completed with the randomly generated training pixels within sets of shapefiles, within the surveyed locations. Classifications were run using six classes for all three altitudes with all data available in the scene. Classifications were run using the 90m multispectral dataset using seven, six and five classes to represent to covers within the imagery. These classifications employed the Maximum Likelihood algorithm. Each classification then underwent an accuracy assessment with a confusion matrix to compare the error within each classification (Jensen, 2005). The various confusion matrices were then compared to consider error amongst different altitudes and training sample selections. Once a classification scheme with a minimum error and an extent that captured the entire area of study was selected, DEMs generation began.

DEMs were generated by isolating the vegetation classes as shapefiles and applying canopy adjustments to respective classes on the DSM. Two methods were employed to determine canopy adjustment values: a flat subtraction method, and a function-based method. The flat subtraction method was produced using mean canopy height of the class at the time of the first vegetation survey. The second method utilized functions portraying relationships between reflection indices and canopy height for a given pixel.

Canopy height was determined by subtracting RTK elevation values from the UAS derived canopy elevation values, at the polygon vertices. These heights were then plotted against remotely sensed variables (e.g., NDVI, NDRE) to examine any relationships that may exist between the two, and their strength. Adjustment functions were generated from the data that exhibited continually increasing function and a strong (>0.7) R value. The raster exhibiting the correlation was then clipped with the respective class shapefile or 'mask', and then transformed

with the respective function, generating a raster of canopy adjustment values. The raster

generated for each class was subtracted from the DSM, generating the DEM.

The results for the adjustments were then compared to elevation values of the origin

points from the vegetation survey. RMSE was then calculated for the adjustments and compared

between DEM generation methods. RMSE was calculated for both DEMs with the following

equation:

$$RSME = \sqrt{\frac{\sum_{i=1}^{n}(P - O)^2}{n}}$$

P is the predicted value, and O the observed value. The DEM generation methods were then

coupled, utilizing the best of each method to produce a DEM with the maximum accuracy. The

RMSE values for the surveyed bare surfaces was then added to the running error count,

producing a final RMSE value for the DEM.

CHAPTER 4

Results

4.1. Vegetation Canopy Heights

The results of the vegetation canopy height surveys are summarized in the following Table 4.1 and Figure 4.1. Survey 1 was completed between August 30th and 31st, while Survey 2 was completed September 13th. The differences between the two surveys revealed growth for all three live classes, and a very slight decline for the dead class. The variation in heights between the two survey averages is depicted with standard error bars, spanning the greatest range for the *S. alterniflora*, and then *J. geradii* alive. The range and mean heights between surveys likewise revealed the most change in the *S. alterniflora* and *J. geradii* alive class; in terms of form they are the more variable and dynamic species in the landscape.

Surveyed Canopy Heights (cm)	Survey 1 Mean	Survey 2 Mean	Δ Mean (S2-S1)	Survey 1 Range	Survey 2 Range	Δ Range (S2-S1)
S. alterniflora	69.6	81.7	12.1	52	60	8
S. patens	8.4	9.4	1	3	5	2
J. geradii Alive	36.3	40	3.7	6	10	4
J. geradii Dead	7.5	7.3	-0.2	3	3	0

Table 4.1 Surveyed Monoculture Canopies Mean and Range

Surveyed Canopy Height Means
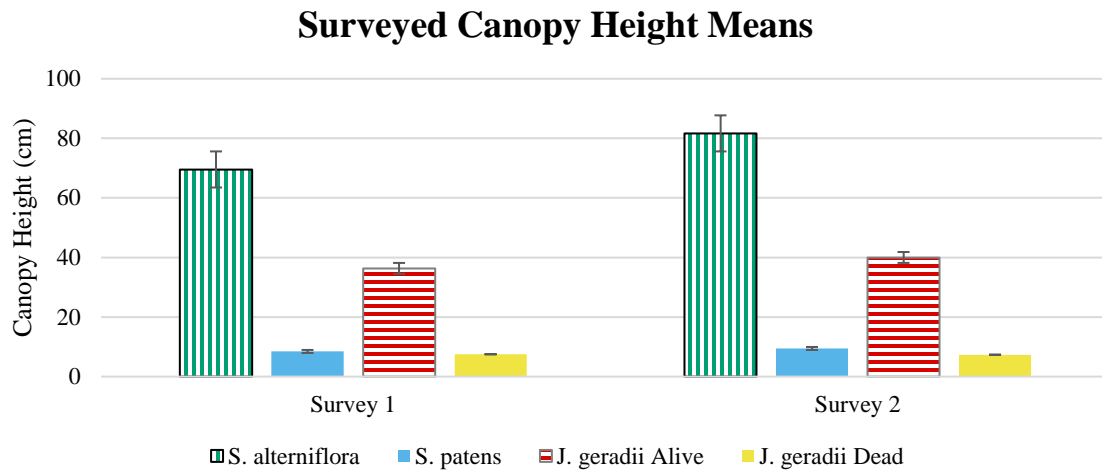
Figure 4.1: Surveyed Canopy Heights Mean

4.2. Pix4D Products

The reports automatically generated from Pix4D gives a variety of information on the structure for motion process which constructs the reflectance maps and DSMs. The following table summarizes the Pix4D projects, allowing for comparison amongst the different datasets. All projects report a relatively low RMSE value for DSM elevation, from 1.6 and 2.6 cm. As the lower flights were unable to capture the entire marsh surface, the number of G.C.P.s and the area covered in those datasets are lower. The file size for the projects ranges 15gb for the 90m RGB to 4.5gb for the 70m multispectral (MS). While the 90m RGB and MS flights cover nearly the same area, the file size for the 90m MS project is roughly two thirds the size of its RGB counterpart.

Project	50m MS	70m MS	90m MS	90m RGB
G.S.D. (cm)	5.26	7.22	9.41	3.84
Extent (ha)	7.36	9.41	19.25	20.29
Number of G.C.P.s	8	7	13	13
RMSE (cm)	1.6	2.2	1.7	2.6
Project File Size (GB)	5.55	4.57	10.2	15

Table 4.2 Pix4D Project Details

4.3. DSM Generation (Bare Surface Validations)

The DSMs generated were assessed with various test points; the results have been

summarised and displayed in the Figures 4.2, 4.3 and Table 4.3. The Root Mean Square Error

(RMSE) method is an independent measure of error as to that generated in the PIX4D report.

Comparing the DSMs generated at various altitudes to the RTK surveyed points at bare surface

locations reveals RMSE is greater for the 50m MS and 90m RGB flight, and lowest for the 70m

and 90m MS flight. Comparing the two 90m imagery sets (more similar spatial extents) with the

figures further emphasises the greater error within RGB imagery set. There exists a

large difference in RMSE values of PIX4D and those measured independently, ranging from

5.4cm to 15.3 cm.
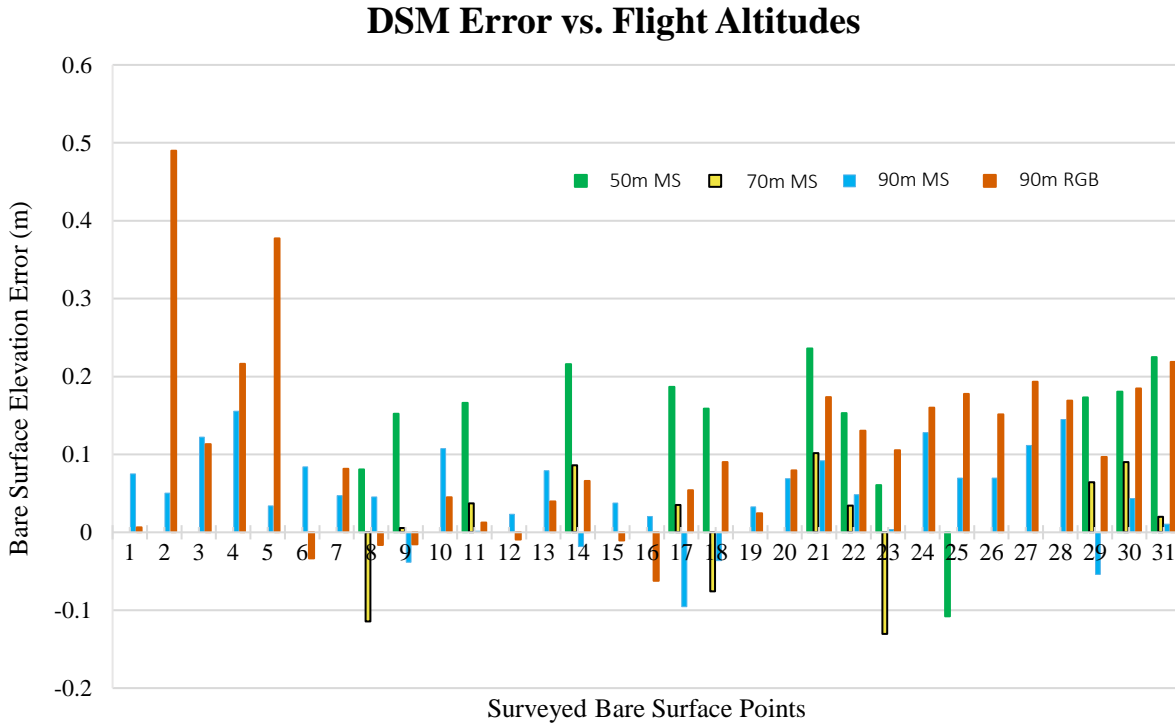
Figure 4.2: DSM Bare Surface Error Per Flight Altitude

90m MS and 90m RGB DSM Error
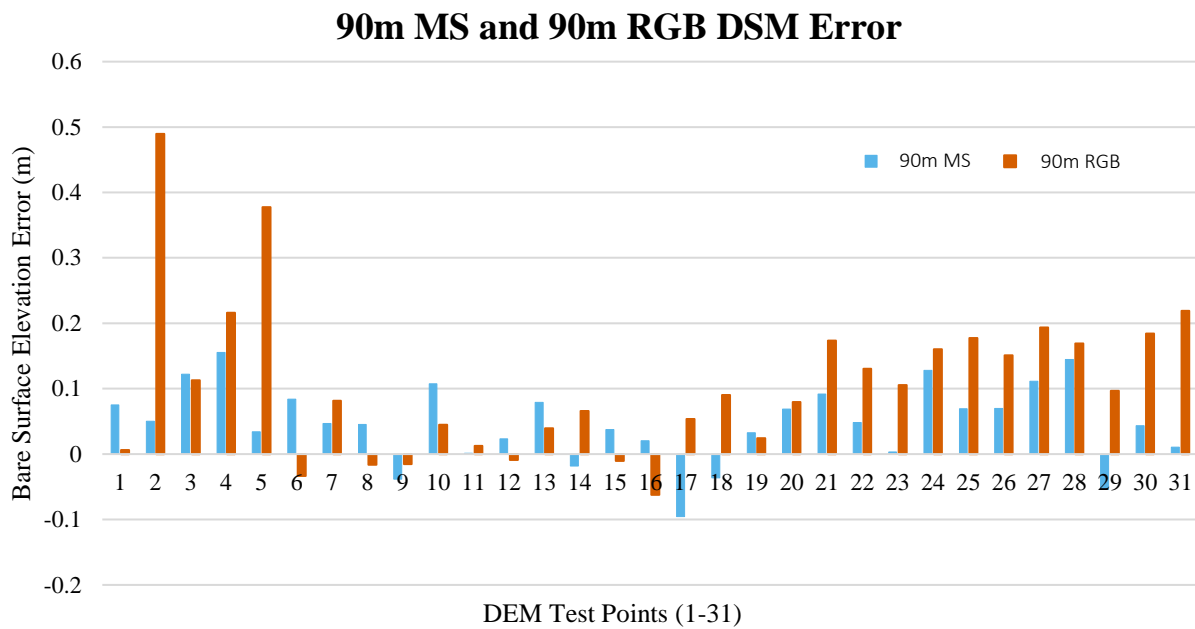
Figure 4.3: Comparison of DSM Error, 90m RGB and MS

Altitude	RMSE (cm) (DSM and RTK Bare Surface Points)	RMSE (Pix4D) (cm) (Pix4D Projection and GCP Points)
50 m MS	16.9	1.6
70m MS	7.6	2.2
90m MS	7.5	1.7
90m RGB	15.8	2.6

Table 4.3: Comparison of DSM Error, Pix4D and Surveyed

4.4. Indices:

Analysis of the NDVI map, Figure 4.4, reveals three distinct regions from foreshore to pasture. The foreshore mud has extremely low NDVI values, appearing dark. The saltmarsh has a low to mid-range of NDVI values and is less bright than the pasture and farmland with the highest NDVI values. There are some very low NDVI values visible as dark patches occurring in the middle of the saltmarsh platform. The NDRE map lacks the contrast the NDVI map provides between saltmarsh and pasture.
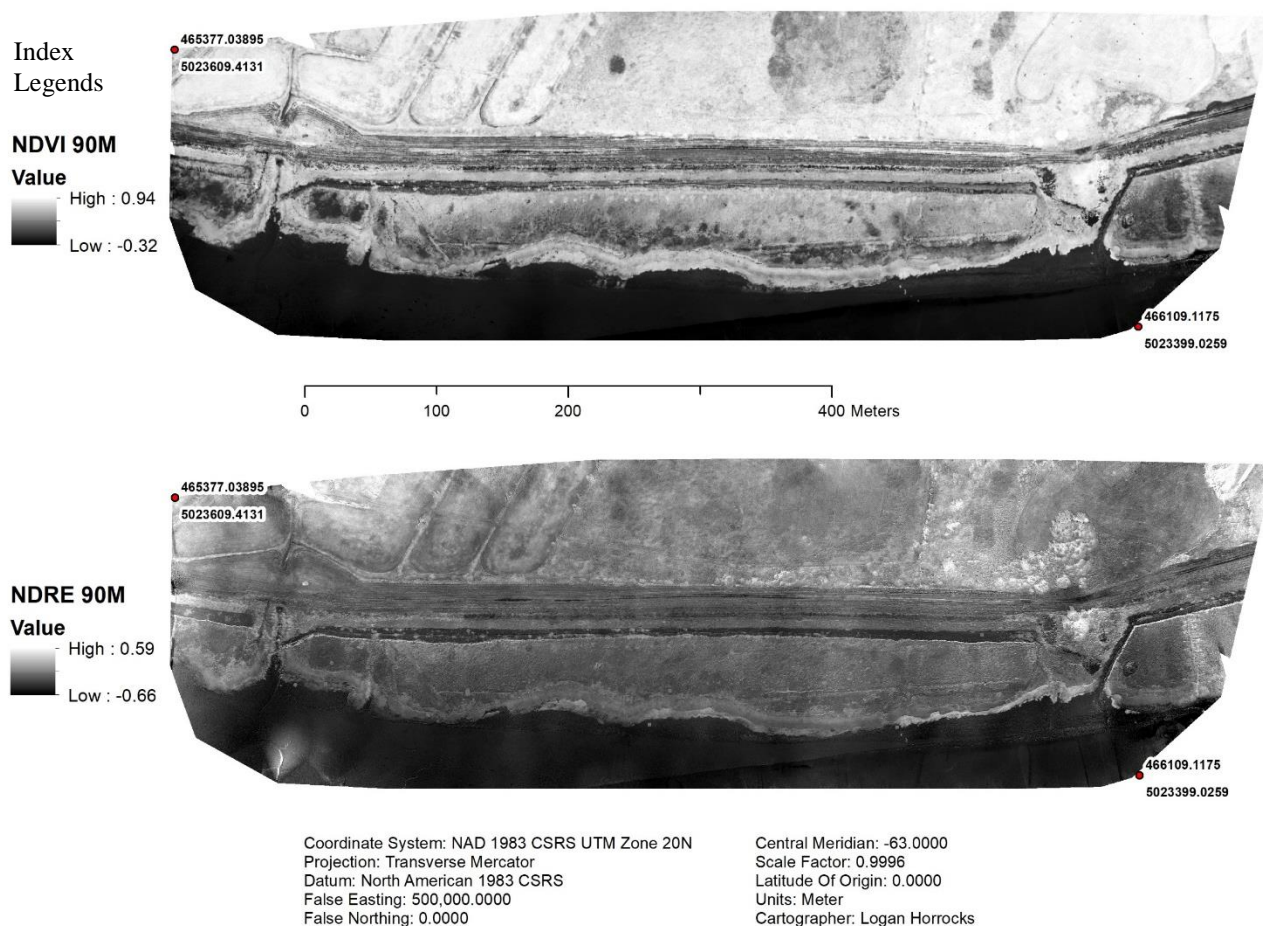
Figure 4.4: NDVI and NDRE Maps generated from 90m MS flight

4.5. Canopy Heights vs. Index Values

The following section summarizes the process in which the relationships for the function-based DEM subtraction were determined. Figures 4.5 (A-F) and 4.6 (A-F) display normalized differential index values on the X axis, and Canopy height (DSM Elevation - RTK elevation) on the Y axis. The trendlines describe a relationship between the variables, while the R values are used to asses the strength of the relationship. Comparison of DSM/RTK derived canopy heights and index relationships reveals a variety of both weak and moderately strong R values.

The figures with a circled letter (Figure 4.5 C&E, Figure 4.6 B) display the functions with moderate R values and a trend of consistent increase (no instance of decrease in canopy height throughout the function); these are the functions utilized for DEM creation. Figure 4.5 E was generated using data from both *J. geradii* classes to obtain a function that that expresses both stages of the species lifecycle. The R value in Figure 4.5 E is higher than all other functions created in attempt to portray a consistently increasing relationship between *J. geradii* and a reflectance index. Rendering the axis of Figure 4.6 B to the same scale as the rest of the figures makes it hard to observe the binomial trendline; resembling a parabola approaching its vertex. The removal of two outliers in Figure 4.6 A to create 4.6 B raised the R value from 0.26 to 0.76.

Most attempts to represent the relationship between canopy heights and reflectance index values yielded functions with low R values as seen in the Figures included in the appendix. Some attempts returned high R values, yet possessed fluctuating trendlines, such as Figure 4.5 D and 4.6 E.
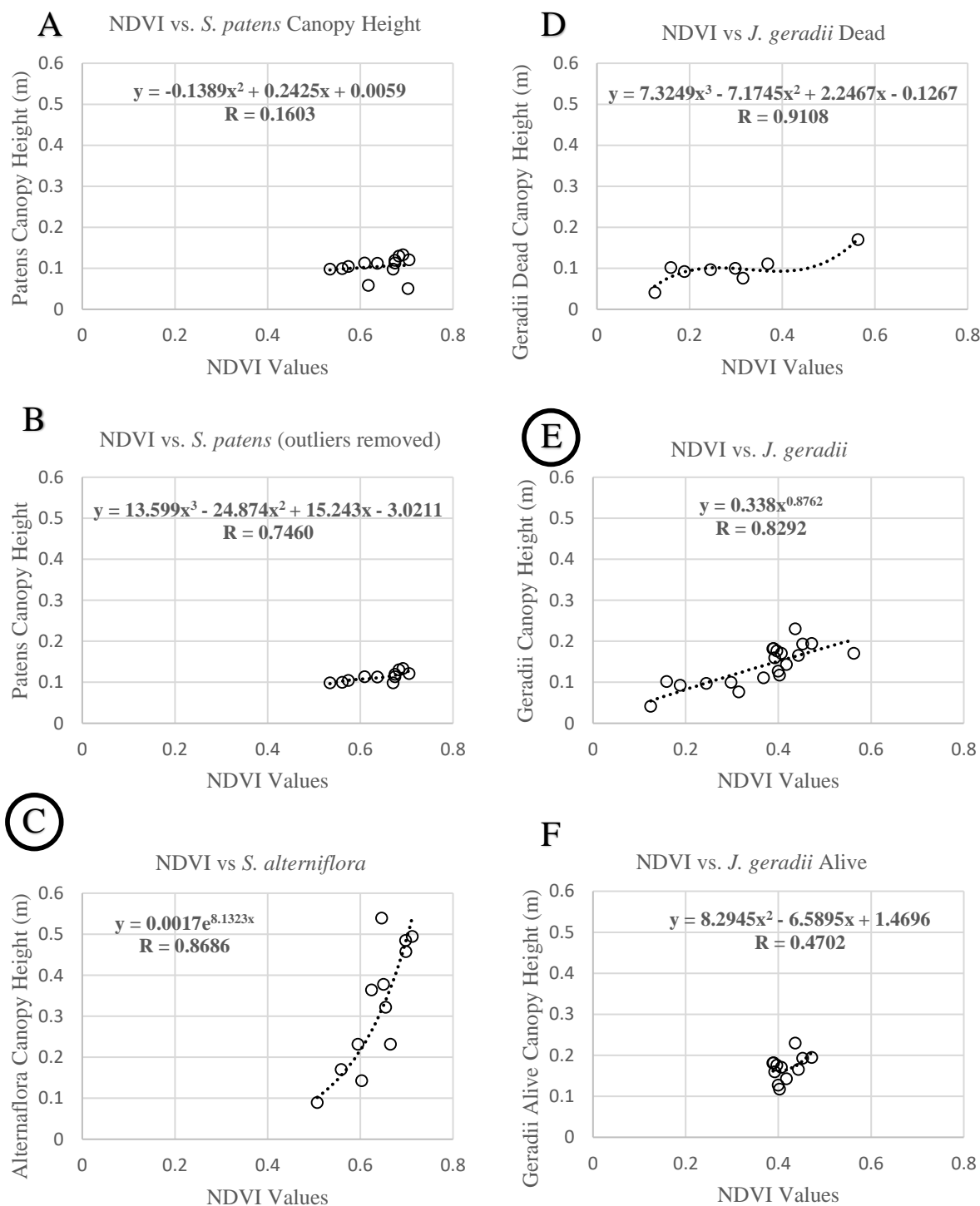
Figure 4.5 (A-F): NDVI Canopy Height Functions. Circled functions used in DEM generation.

A — NDRE vs S. patens

$$y = -485.11x^3 + 218.29x^2 - 31.639x + 1.5812$$
$$R = 0.5119$$

D — NDRE vs. *J. geradii* Alive

$$y = 25.038x^2 - 8.1733x + 0.8274$$
$$R = 0.3434$$

B — NDRE vs *S. patens* (outliers removed)

$$y = -12.065x^2 + 4.3375x - 0.2604$$
$$R = 0.8761$$

E — NDRE vs. *J. geradii* Dead

$$y = 228.09x^2 - 51.235x + 2.9305$$
$$R = 0.9186$$

C — NDRE vs. *S. alterniflora*

$$y = 3.173x - 0.136$$
$$R = 0.5143$$

F — NDRE vs. *J. geradii*

$$y = 1.6987x^{1.2751}$$
$$R = 0.6383$$
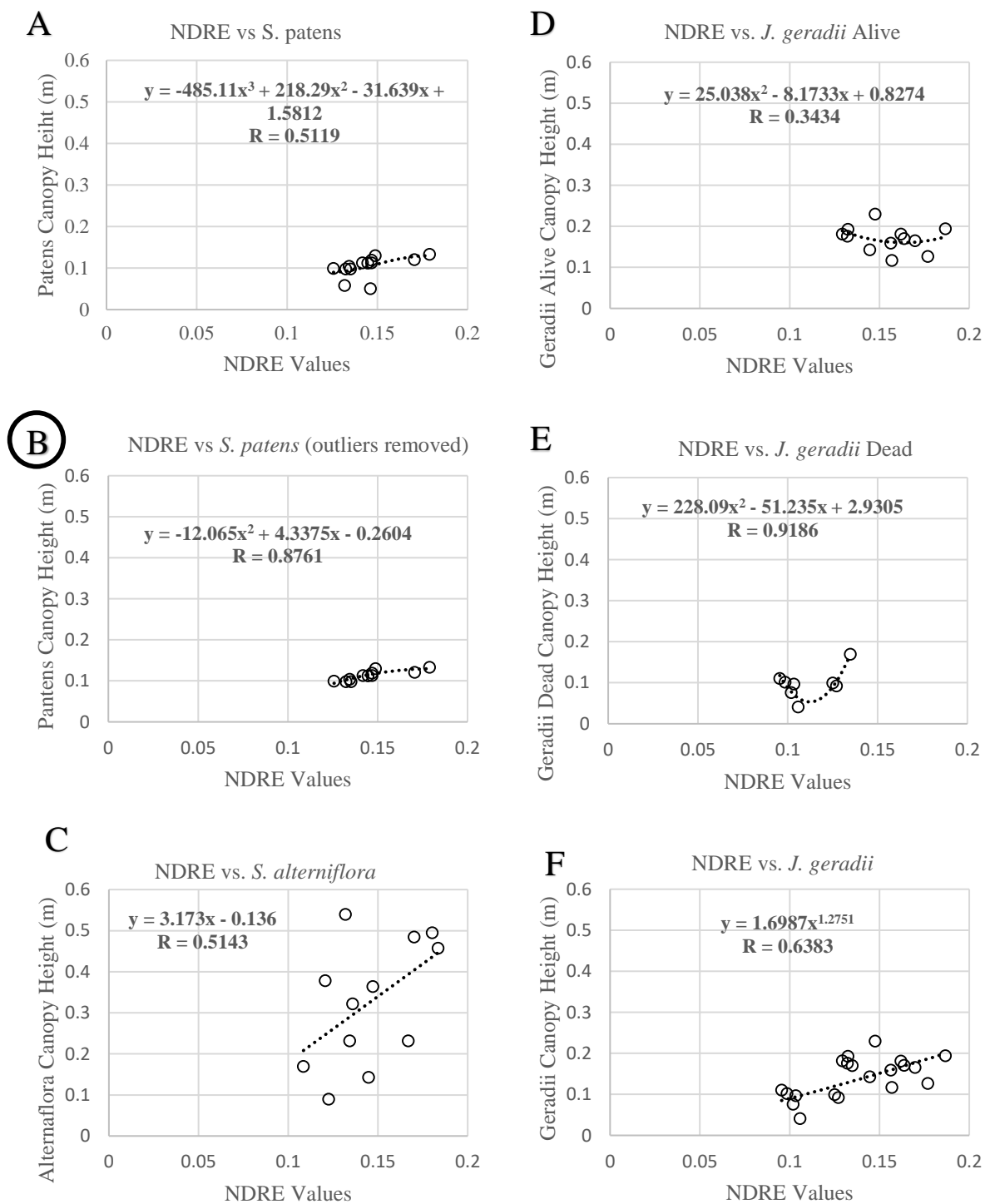
Figure 4.6 (A-F) NDRE Canopy Height Functions. Circled function used in DEM generation.

4.6. Isocluster Classification

Isocluster classifications with various parameters were completed on the 90m MS dataset to make some initial observations about the data and its potential. The following Figures 4.7 and 4.8 are the results of an eight class Isocluster classification using the 90m MS DSM, reflectance maps, NDVI and NDRE as input rasters.

This initial classification managed to separate several key features out of the dataset, while classifying several unique features into the same class. For example, class 4 contains the *S. alterniflora* patches, borrow pits and a large section of pasture in the upper right of the map. Class 6 contains the high marsh community on the marsh platform and some patches of shrub and tree community in the upper half of the map. To further examine the classification, a black delineation of the foreshore from 2017 was applied over the map. As seen on Figure 4.7, the divide between classes 3 and 4 seems to portray the foreshore/saltmarsh edge. Shown in Figure 4.8, the divide between classes 4 and 5 seems to correspond to the saltmarsh/burrow pit edge, and the *S. alterniflora* and *S. patens* zones.
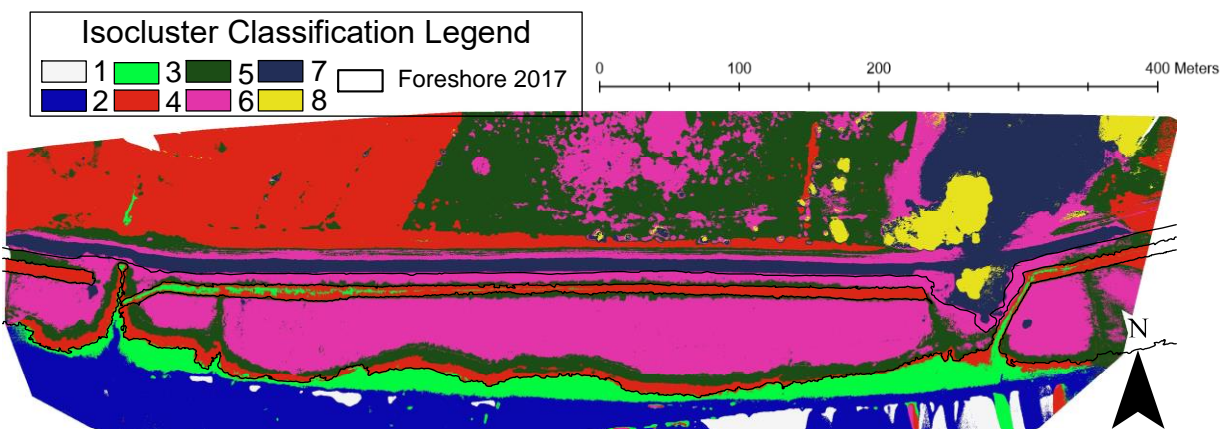
Figure 4.7: Isocluster Classification, 90M MS
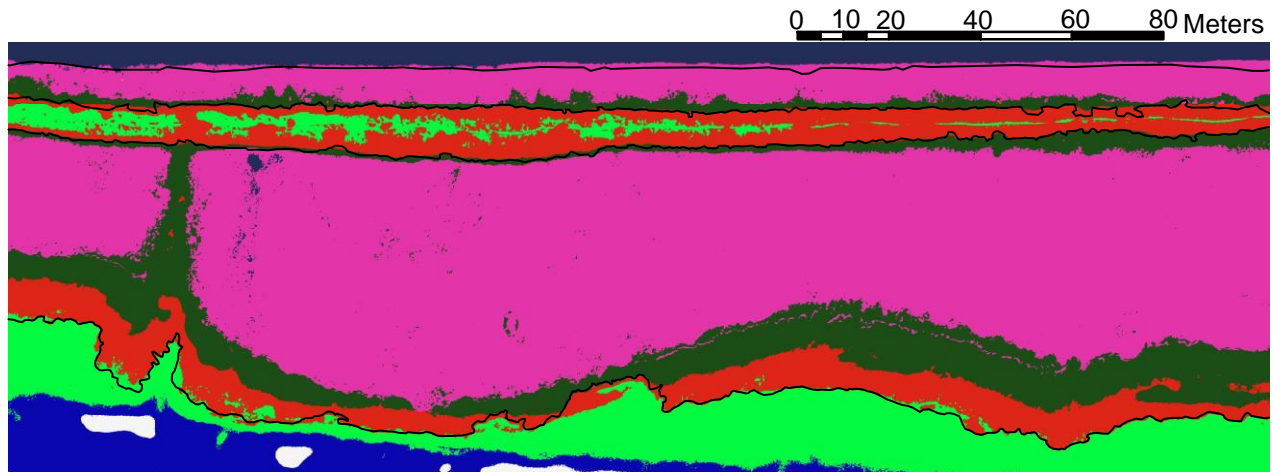
Figure 4.8: Isocluster Classification, 90M MS, Saltmarsh and Borrow Pit

4.7. Supervised Classifications and Confusion Matrices

Confusion matrices are implemented to assess error in the supervised classification process. The tool generates a chosen number of points within the map, for each class, where the cover is known. The tool then evaluates whether the classification assigned that point correctly, and if not, which class was there. The confusion matrix displays the classification data in the primary column, and the reference data in the top row. The matrix has several key attributes: overall accuracy, producer's accuracy, user's accuracy and the kappa coefficient. Overall accuracy is the quotient of correctly classified pixels and the total number of pixels utilized in the confusion matrix (Jensen, 2005). Overall accuracy is displayed at the intersection of producer's accuracy and user's accuracy. Producer's Accuracy is a measure of omission, indicating how accurately reference pixels were classified (Jensen, 2005). It is calculated with the quotient of correct pixels in a class and the total number of reference pixels for that class. User's accuracy is a measure of commission, indicating the likelihood of a classified pixel properly representing the

land cover (Story and Congalton, 1986; Jensen, 2005). It is calculated with the quotient of correct

pixels in a class and the total number of pixels assigned into the class (Jensen, 2005). The kappa

coefficient is indicative of the agreement between the reference data and the classification map

(Congalton, 1991, Jensen 2005). In its generation, both chance agreement and the overall

accuracy are taken into account (Rosenfield and Fitzpatrick-Lins, 1986; Congalton, 1991; Jensen,

2005). The tables are in part summarized by the kappa coefficient, a measure of how well the

classification map fits the surveyed data. The number of test points was set to 1600 for each class

in the following matrices comparing different flight altitudes but varied based on what was

captured within the respective flight.

4.7.1 Supervised Classifications and Confusion Matrices: Varying Flight Altitudes

As shown in the three confusion matrices, there is very little difference in the kappa

coefficient amongst the three flight altitudes. All classifications possess very high kappa

coefficients ranging from 0.98 to 1. Amongst these classifications, user and Producer's Accuracy

errors occur mainly in the *J. geradii* classes. Table 4.4 displays the multispectral 90m, six class

classification utilized in DEM creation.

Class Value	Alterniflora	Patens	Geradii Alive	Geradii Dead	Mud	BP	Total	User's Accuracy	Kappa
Alterniflora	1600	0	0	0	0	0	1600	1	
Patens	6	1594	0	0	0	0	1600	0.9962	
Geradii Alive	0	0	1498	102	0	0	1600	0.9363	
Geradii Dead	0	0	0	1600	0	0	1600	1	
Mud	0	0	0	0	1600	0	1600	1	
Borrow Pit	0	0	0	0	0	1600	1600	1	
Total	1606	1594	1498	1702	1600	1600	9600	0	
Producer's Accuracy	0.9962	1	1	0.94	1	1	0	0.9887	
Kappa									0.9865

Table 4.4:Confusion Matrix, 90m MS, 6 Classes

Class Value	Alterniflora	Patens	Geradii Alive	Geradii Dead	Mud	BP	Total	User's Accuracy	Kappa
Alterniflora	740	0	0	0	0	0	740	1	
Patens	0	1099	0	0	0	0	1099	1	
Geradii Alive	0	0	1034	0	0	0	1034	1	
Geradii Dead	0	0	0	758	0	0	758	1	
Mud	0	0	0	0	1118	0	1118	1	
Borrow Pit	0	0	0	0	0	841	841	1	
Total	740	1099	1034	758	1118	841	5590	0	
Producer's Accuracy	1	1	1	1	1	1	0	1	
Kappa									1

Table 4.5: Confusion Matrix, 70m MS, 6 Classes

Class Value	Alterniflora	Patens	Geradii Alive	Geradii Dead	Mud	BP	Total	User's Accuracy	Kappa
Alterniflora	740	0	0	0	0	0	740	1	
Patens	0	590	0	0	0	0	590	1	
Geradii Alive	0	0	550	15	0	0	565	0.973	
Geradii Dead	0	0	0	758	0	0	758	1	
Mud	0	0	0	0	1118	0	1118	1	
Borrow Pit	0	0	0	0	0	841	841	1	
Total	740	590	550	773	1118	841	4612	0	
Producer's Accuracy	1	1	1	0.981	1	1	0	0.996	
Kappa									0.996

Table 4.6: Confusion Matrix, 50m MS, 6 Classes
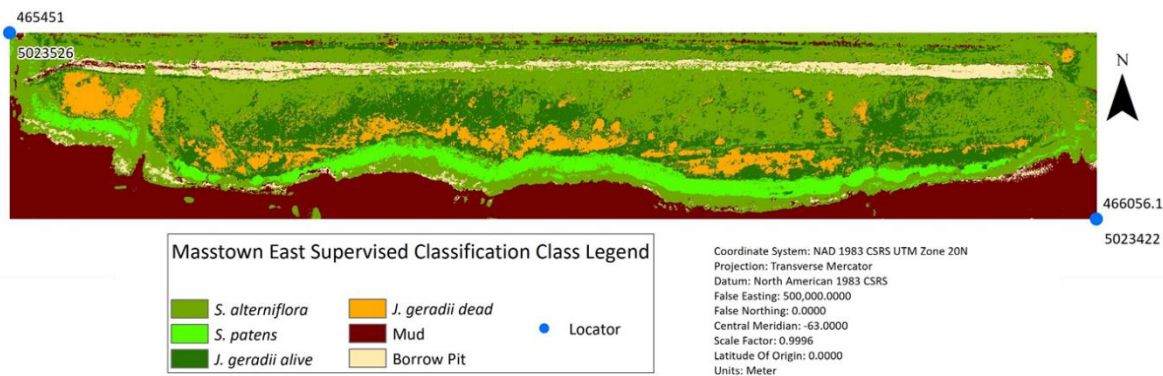
Figure 4.9: Supervised Classification, 6 classes, 90m multispectral

As a means of assessing the training data distribution, a classification was performed with one third of the training data of all previous classifications. The kappa coefficient of this classification is relatively lower than all other classifications, at 0.80. The major source of error in this classification is found within the borrow pit class, with a Producer's Accuracy of 0.14. The 430 borrow pit and 41 *J. geradii* pixels placed in the mud class result in its kappa coefficient of 0.51.

Class Value	Alterniflora	Patens	Geradii Alive	Geradii Dead	Mud	Borrow Pit	Total	User's Accuracy	Kappa
Alterniflora	493	0	0	0	0	0	493	1	
Patens	7	500	0	0	0	0	507	0.986	
Geradii Alive	0	0	496	0	0	0	496	1	
Geradii Dead	0	0	4	459	0	0	463	0.991	
Mud	0	0	0	41	500	430	971	0.514	
Borrow Pit	0	0	0	0	0	70	70	1	
Total	500	500	500	500	500	500	3000	0	
Producer's Accuracy	0.986	1	0.992	0.918	1	0.14	0	0.839	
Kappa									0.807

Table 4.7: Confusion Matrix using Cell C as training data, 90m, 6 classes

4.7.2. Supervised Classifications and Confusion Matrices: Varying Test Pixel Locations

Tables 4.8 and 4.9 detail classifications performed with five classes instead of six, as the Mud and Burrow Pit classes were merged. The classifications were performed with alternating testing and training datasets. The first classification was performed with training data selected from Cell C, and validation data from Cell A and B, the second was performed with the alternative. The confusion matrices produced from these classifications both reveal very high kappa coefficients, although that of the classification performed using training data from Cell C was slightly larger. Errors occurred predominately in the *S. alterniflora* and Mud class between

the two classifications, with errors having occurred in the *J. geradii* in either state. Among the

two classifications, the *S. paten*s class contains the least error.

Class Value	Alterniflora	Patens	Geradii Alive	Geradii Dead	Mud	Total	User's Accuracy	Kappa
Alterniflora	469	0	0	0	0	469	1	0
Patens	5	500	0	0	0	505	0.990	0
Geradii Alive	0	0	493	0	0	493	1	0
Geradii Dead	0	0	7	483	0	490	0.986	0
Mud	26	0	0	17	500	543	0.921	0
Total	500	500	500	500	500	2500	0	0
Producer's Accuracy	0.938	1	0.986	0.966	1	0	0.978	0
Kappa	0	0	0	0	0	0	0	0.972

Table 4.8: Confusion Matrix using Cell C as training data, 90m, 5 classes

Class Value	Alterniflora	Patens	Geradii Alive	Geradii Dead	Mud	Total	User's Accuracy	Kappa
Alterniflora	73	0	0	0	8	81	0.901	0
Patens	0	86	0	0	0	86	1	0
Geradii Alive	0	0	82	0	0	82	1	0
Geradii Dead	0	0	5	78	0	83	0.939	0
Mud	0	0	0	0	168	168	1	0
Total	73	86	87	78	176	500	0	0
Producer's Accuracy	1	1	0.942	1	0.954	0	0.974	0
Kappa	0	0	0	0	0	0	0	0.966

Table 4.9: Confusion Matrix Using Cell AB as Training data, 90m, 5 classes

4.8. Comparing Class Extents

The extents for each class within the supervised classifications were converted into

percentages showing how much of the scene each made up respectively. Percentages were

determined by dividing the number of pixels in the class by the total number of pixels in the

scene and multiplying by 100.

4.8.1. Comparing Class Extents: Varying Flight Altitudes

Figure 4.9 displays percentages for each class in the varying altitude supervised classifications with six classes. The *S. patens* and Borrow pit classes remain consistent across all the classifications, accounting for 6-11% and 1-5% of the scenes. The mud class remains moderately consistent while changing altitudes, within the range of 16-24% of the scene. The *J. geradii* dead and Borrow Pit classes near disappear in the 70m MS classification, yet *J. geradii* dead accounts for 19% of the scene in the 50m classification. The *S. alterniflora* and *J. geradii* alive class extents vary greatly across the different altitude flights, from 6-41% and 19-65% of the scenes, a difference of 35% and 46% respectively.
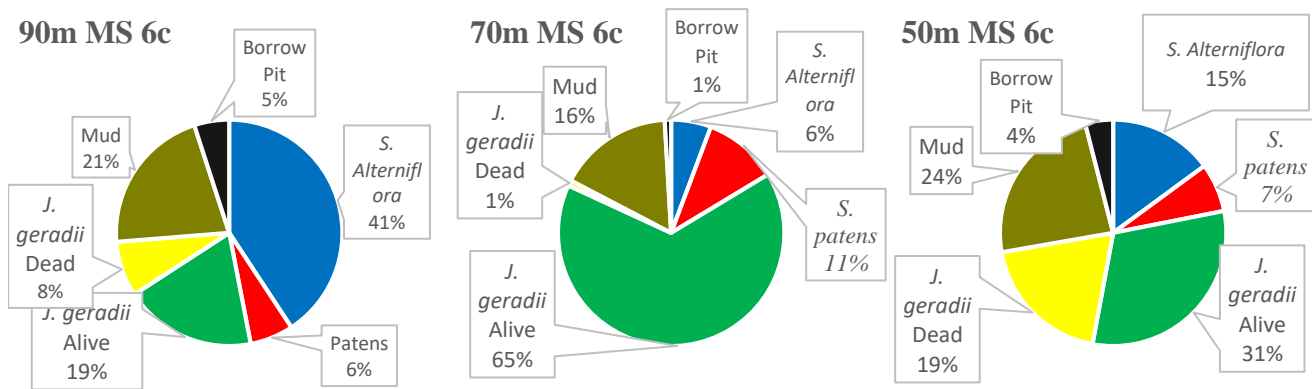
Figure 4.10: Class Extents for 50, 70 and 90m multispectral Supervised Classifications, 6 classes.

4.8.2. Comparing Class Extents: Varying Test Pixel Locations

Figure 4.10 displays the class extents for the supervised classifications performed on the 90m MS dataset using five classes and alternating the selection of testing and training pixels. The Borrow Pit class that was in previous classifications was combined with the Mud class. The classifications both portray the *S. patens* class as 7% of the total scene. Between these classifications there is a 5% difference in the Mud class, and a 7% difference in the *J. geradii*

Dead class. There is a greater difference in the extents of the *S. alterniflora* and *J. geradii* alive

classes between classifications, 13% and 15% respectively.
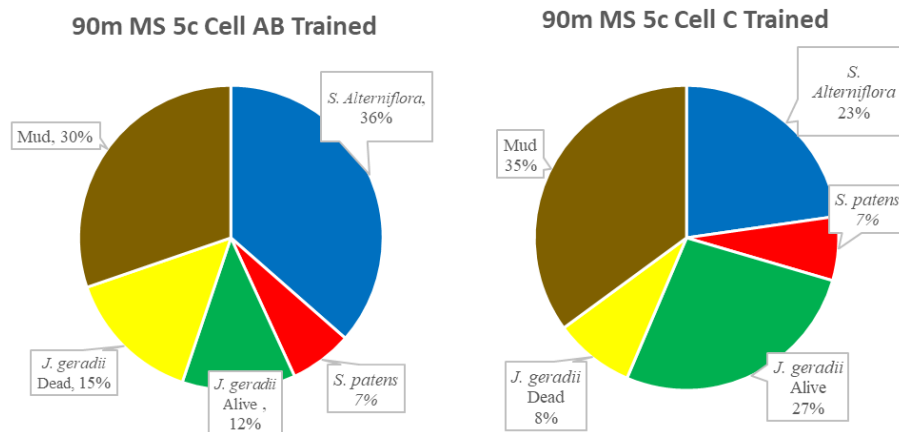
Figure 4.11:Class Extents for Varying Test Pixel Location, 90m multispectral Supervised Classifications, 5 classes.

4.9. DEM Generation

4.9.1 Class Masks

Having performed the classifications and comparing the accuracies amongst them, the

90m flight shows the greatest extent with a minimal sacrifice of accuracy. The 90m dataset has

thus been selected for use in DEM creation. Figure 4.11 is a display of the class-shapes extracted

from the 90m MS, six class classification. These class shapes or 'masks' were used for to subtract

the canopy heights, thereby generating a DEM.
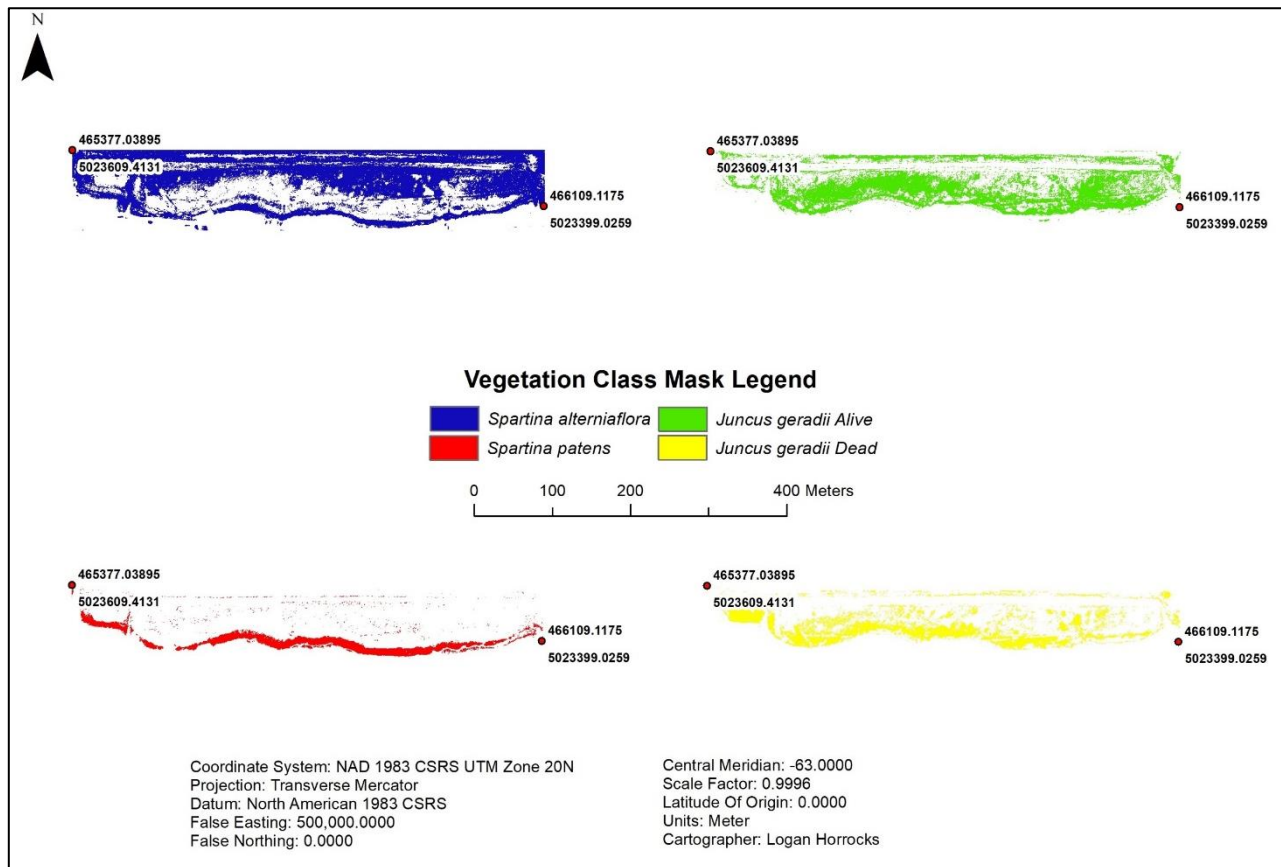
Figure 4.12: Class Masks Derived from the 90m, 6 Class Supervised Classification

4.9.2. DEM Error

Following the generation of DEMs with both the Flat canopy subtraction and Canopy Function methods, DEM error was assessed. DEM error was calculated by subtracting the DEM elevation value from the known elevation value in a variety of locations. Error in the positive indicates where the DEM underestimated elevation, and therefore overestimated canopy height. Error in the negative indicates where elevation was overestimated, and canopy height

underestimated. Figure 4.12 displays the error (in cm) for both DEM generation methods at origin point locations. There is greater error and higher extremes in the flat canopy subtraction method than its counterpart. The flat canopy DEM has maximum error near 60cm, while the canopy function DEM error reaches a maximum near 30cm. Both DEMs display more error in the positive than the negative, indicating canopy height was more often overestimated than underestimated. RMSE was calculated for both DEMs by squaring the error at each point, obtaining the average, and square rooting the product. RMSE of the flat canopy subtraction DEM was nearly double that of the canopy function DEM, at 25cm and 13cm respectively.

DEM VALIDATIONS (Origin Points)
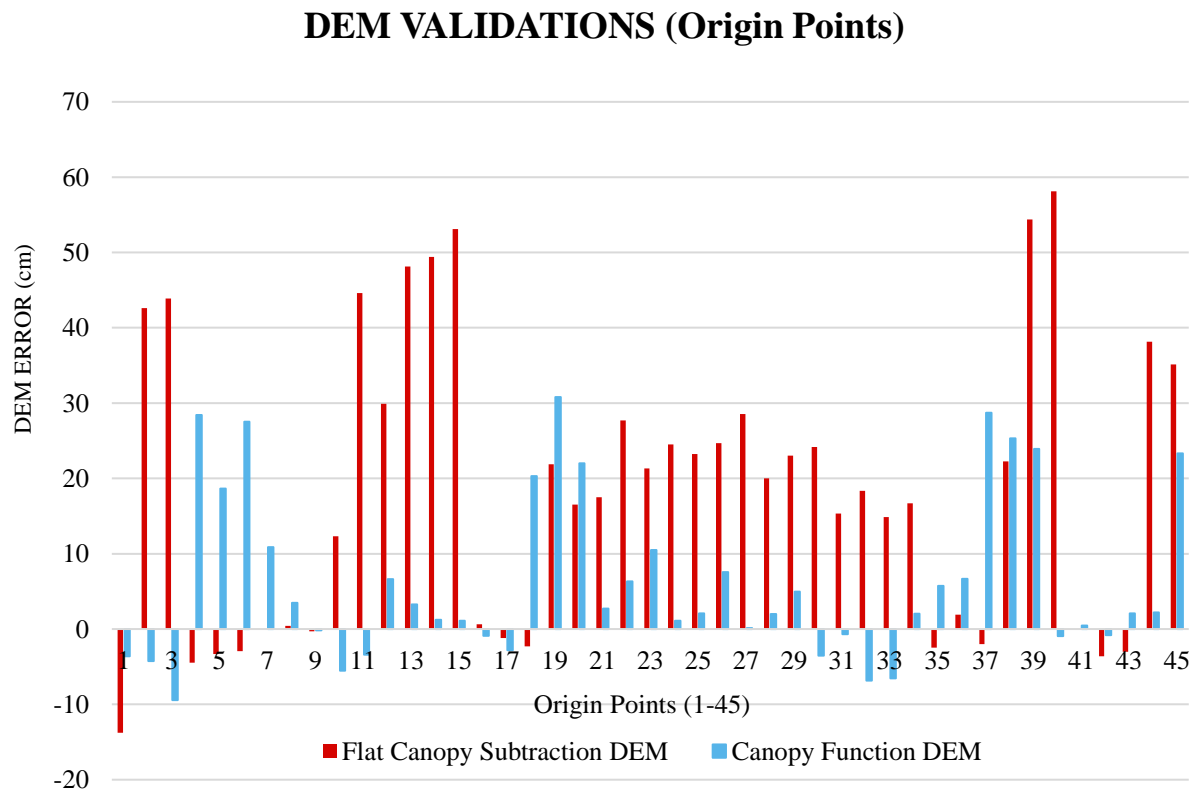
Figure 4.13: Comparison of DEMs Error at Origin Point Locations

4.9.3. Calculating RMSE per Class

RMSE was calculated for within the DEMs for each of the landcover classes to compare how accurately each method represented individual classes. Table 4.10 displays the RMSE within each class for both DEMs, and total RMSE at the bottom. The second column displays RMSE for the flat subtraction DEM calculated with Origin points, while the third is calculated with Vertex points. The fourth column displays RMSE per class for the function method DEM. The flat subtraction method most accurately portrays the *S. patens* class, while the other three vegetation classes are best represented with the function method. The fifth and sixth column represent 'Post Results' of the project. The fifth column represents a DEM crafted with the *S. patens* class of the first method, and all other classes using the second. The total RMSE for the resulting 'coupled' DEM is 6cm, roughly half that of the function method DEM. The sixth and final column adds the RMSE of the bare surfaces to the DEM to further assess the surface portrayal. RMSE does not significantly change with the addition of the Bare surface validation points, retaining a value of 6cm.

	Results			Post Results	
RMSE PER CLASS (cm)	**Flat Subtraction DEM (Origin points)**	**Flat Subtraction DEM (Vertex points)**	**Function Subtraction DEM (Origin points)**	**Flat and Function Subtraction DEM (Origin and Vertex points)**	**Flat and Function Subtraction DEM (Origin, Vertex and Bare Surface)**
S. alterniflora	35	44	9	9	9
S. patens	5	4	24	4	4
J. geradii **Alive**	20	16	3	3	3
J. geradii **Dead**	1	5	3	3	3
Bare Surface RMSE	NA	NA	NA	NA	7
RMSE TOTAL (cm)	26	25	13	6	6

Table 4.10: Comparing DEM RMSE per Class

CHAPTER 5

Discussion

5.1. Project Review

This research sought to determine what combination of parameters for a multispectral equipped UAS would yield the most accurate and useful land cover classifications and DEMs for the saltmarsh landscape. This section sequentially investigates the various components of the project and their role in the achievement of the final goal. In the generation of the suite of geospatial products, error compounds, and must be reduced at each step along the way (Jensen, 2005; Carrivick *et al*., 2016). The individual aspects of the project have been discussed in terms of their successes, the assumptions they rely on, and the limitations they are constrained by. Suggestions for improvements, future directions and considerations have been included for each of these aspects. This project was able to produce a final DEM with an RMSE comparable to that of its source DSM, 6cm.

5.2. Field Work and Ground Truthing

The vegetation surveys were completed in two sets, the first on August 30th and 31st, and the second on September 13th. The vegetation and topographic surveys would both have benefited from a more rigorous sample set up. Effort would have been better spent capturing more training/testing data than completing formal vegetation surveys. For this type of ground truthing, a simple validation of homogenous cover, DGPS survey and image would suffice. The formal

survey can take upwards of a half hour if multiple species were present. Those surveys were not used because of the significant diversity at those locations and the impact of mixed pixels on the classification (Jensen, 2005). This type of project may also benefit from a combination of formal and informal validations. A few formal validations would be performed followed by many informal validations, all surveyed with DGPS. In this case, species could be surveyed on the fly as one discovers it in a site. The canopy sampling method is somewhat subjective when trying to determine the mean canopy height for sparser and tall growing vegetation.

The vegetation showed greater variability within the *S. alterniflora* and *J. geradii* Alive. These classes had a greater range and change in canopy height between the surveys than *S. patens* and *J. geradii* Dead classes. These findings compare to other studies examining the species (Smith et al., 1980; Möller, 2006). The growth for all live classes and decline in height for the dead class between surveys confirm their described states.

Drone flights were completed with varying degrees of difficulty. The 90m RGB flight was easy to accomplish, the UAS working as it was supposed to. The flights with the Parrot Sequoia sensor were far less user friendly and required several test flights for trouble shooting purposes. The issue remained an inability to completely load a mission grid, resulting in the craft hovering in a fixed location and wasting battery. As a result, all the multispectral flights were flown manually. The 90m MS flight was completed quickly with two batteries. The 50 and 70m MS flights would have taken more time than was available to cover the entire marsh surface, thus 50 and 70m were only flown for half the site. These lower altitude flights cover less area, capture fewer G.C.P.s while requiring them to be closer together (MP_SpARC, 2017), but deliver a smaller G.S.D.. Radiometric calibration is less accurate for longer flights as more time elapses

between the calibration image and last image in the flight set; meanwhile illumination conditions change. Considering the feasibility, time, and resources, the slight improvements in G.S.D. do not merit flying at lower altitudes in the saltmarsh landscape.

5.2. Pix4D: DSM Production and Limitations

The SFM-MVS processing supplied via the Pix4D software was user friendly and easy to follow. The outputs were generated relatively fast; each project was processed within a night. The subscription fee for the Pix4D software is expensive but facilitates much of the SFM-MVS processing, requiring the user to set the project parameters and georectify. The software is a bit of a black-box with some algorithms and processes not fully disclosed. This is not surprising given the developing nature of SFM-MVS software (Carrivick *et al*., 2016). Considering the Pix4D reports, the 90m MS delivered best ratio of coverage to file size, but at the sacrifice of G.S.D.

The RMSE reported from Pix4D was inconsistent with independently measured RMSE values. Reported RMSE values ranged 5-15 cm less than the independently measured bare surface points. Validation points on the edge of the 70 and 50m DSMs were removed as the significantly higher values were due to the impact of the bowl like warp that exists on the edge of the DSM (MP_SpARC, 2017). Removing these outliers brought down the RMSE of the 50 and 70m flight from 30 and 40cm to their current 15 and 7cm. There was more error in the 90m RGB than 90m MS which came across a slightly surprising. The difference in error may be a product of the georectification process. In the 90m RGB dataset, the center of G.C.P. flag may appear as 1,2,4 or 9 pixels. In the 90m MS dataset it usually shows up as 1 or 4 pixels, making it much

easier for the user to remain consistent throughout the process (Jensen, 2005). Error was most similar between the 90m RGB and 50m MS set, and between the 70 and 90m MS sets. This may suggest that reducing flight altitude (thereby reducing G.S.D) may be related to increased error.

5.3. Generation of Indices and Canopy Height Statistics

A brief visual analysis of the indices shows the NDVI has more contrast amongst features, while the NDRE appears very grey and somewhat noisy. There seems to be some brightness banding in the NDRE which may be an artifact and sunlight reflecting off the wet mud surface. NDRE is supposed to reveal crop health in late season (Spiral Commercial Services, 2015; MicaSense, 2017), yet there is not nearly as much variation in the marsh platform in NDRE as in NDVI. This is especially true for the center high marsh region *where J. geradii* is found both dead and alive. NDVI portrays the contrast between dead and alive *J. geradii*, suggesting perhaps NDRE is not as effective in observing saltmarsh phenology as the maturation of crops.

The creation of functions for the DEM adjustment values operates under the assumption supported by Medeiros *et al.*, (2015); as canopy height (and thus biomass) increases, so should reflectance, or brightness in the respective index. An ideal function would reach an asymptote as the maximum canopy height was reached and would possess a high R value (greater than 0.7), indicating a strong effect size (Moore et al., 2013). Simpler functions were sought, giving preference to linear and exponential functions over polynomial ones.

The DEM creation could have benefited from the use of more points for determining relationships; more vegetation survey points with elevation values would allow for this. These

functions should employ 20-30 points per class, greater than the minimum population sample size (10 points per class) required for regression analysis (Statistics Solutions, 2018).

Strong R values were observed for some trends, but trends fluctuated as NDVI and NDRE increased. It was deemed fluctuations contradicted the assumption the relationships operated upon and are thus not used (Medeiros *et al*., 2015). In hindsight, fluctuations may have been the result of training site locations where the vegetation is blown over or laying down rather than upright (accounting for low canopy heights), thus exposing more of the plants surface to the sky above (accounting for higher index values). Outliers were removed from the *S. patens* class as the canopy height values did not correspond to those measured manually. It proved difficult to observe a strong relationship between the two variables for the *S. patens* class. *J. geradii* alive and dead proved difficult to derive functions for that didn't fluctuate or have a low R value. *J. geradii* classes were then combined as they are the same species, producing an ideal trend line with a strong R value.

5.4. Land Cover Classifications, Confusion Matrices and Class Extents

The Isocluster classification proved effective for delineating the marsh/foreshore boundary as seen with the 2017 foreshore line. The classification incorrectly classifies some features, for example the vegetation in Figure 4.7 between the dyke road and ditch is classified the same as the high marsh region. The low marsh region is portrayed with lime green, red and dark green. In Figure 4.8, the red area in front of the marsh corresponds roughly to the *S. alterniflora* zone, and the dark green to the *S. patens*. The pasture behind the dyke is largely represented with the red and dark green classes. This may reflect the influence of the DSM on the

classification (Roe, 2016). Overall, the Isocluster classification displays promise for further accurately classifying the data

It is recognized that the sample set up was not as extensive as it could have been and speaks to the balance of a robust sample set up, and what is physically possible. Classification kappa coefficients reflect a sample set up that could have been more robust with their very high values. Attempts were taken to assess the sample set up by varying and using portions of the training and testing data. In all supervised classifications produced, there is salt and pepper effect.

The notion that one of the classifications scored a kappa coefficient of 1 sparks the interest to re-perform the classifications with a more robust training sample set up, as this result seems unobtainable (Jensen, 2005). All confusion matrices seem to demonstrate very high kappa coefficients, suggesting classifications accurately performed at the test point locations. The changes in altitude do not seem to have an impact in classification accuracy. These high kappa coefficients are likely a reflection of the training and testing pixel locations (Jensen, 2005).

The next method used to assess the capacity of the training data was alternating test pixel locations. The classification run using six class and training data only from Cell C reveals a kappa coefficient of 0.8, a relatively successful classification (Jensen, 2005). The successes of the classification suggest that there is validity to the training sample set up, as a relatively successful map can be performed with one third of the input data.

High kappa coefficients were observed for the 90m 5 class classifications which employed alternating training and testing data. One classification utilized Cell AB and training data and cell C as validation, while the other utilized the opposite. The high kappa coefficients suggest further classifications can be successfully performed with one to two thirds of the

training data (Jensen, 2005). Future studies should contain more testing and training sites scattered across the area of study if not constrained by time or resources.

Analysis of the class extents reveals one species that remains remarkably consistent across the scenes, while all other classes vary greatly. *S. Patens* remains near 7% for all classifications with alternating inputs. It seems unusual that two classes represent so little of the scene in the 70m MS scene, at 1% each. There is a greater variance in extents when changing altitudes than when changing training sample data, shown in the difference between the first three, and then the second two. The reduction in variance among class extents for the latter two classifications suggests the 90m flights with alternating input data more similarly portray the surface than the flights of varying altitude.

Regarding the research question, all altitudes have produced classifications of a very similar accuracy, well within the desired ranges of error. The aim was to produce a classification with a high User's Accuracy and a kappa coefficient greater than 80%, as it indicates strong agreement between the classification and test data (Jensen, 2005). The question now considers which combination of parameters will yield the most useful classification. To answer this question, the extents (the area covered by each flight) and the flight time have been considered for each flight. The latter two flights (50 and 70m) do not display the same extent as the 90m flight as they were unable to cover the entire site in the given time. When considering the utility of UAS for mapping of these covers, the duration of time spent flying should be minimized to reduce variations in conditions across the scene (Aber et al., 2010). Thus, a 90m altitude flight that covers twice the area of a 50m flight in the same time span is favorable. Higher altitude flights result in smaller datasets to cover a common extent, requiring less time and computational

power to process, thus reducing time associated costs (Colomina and Molina, 2014; Crutsinger *et al*., 2016). Considering the similar accuracy outputs from these flights, the difference in extents and processing resources suggests the 90m flight produces the most useful land cover classification.

5.5. DEM Generation: Assumptions, Constraints and Error

      The two methods of DEM generation proved fruitful. Each method operates with its own assumption and is thus limited in one or another. The flat canopy subtraction assumes a static nature to a class, e.g., all *S. alterniflora* is 69 cm. The function canopy subtraction assumes a more dynamic and variable nature to a class, and compensates accordingly (Medeiros *et al*., 2015). It was predicted the latter method would better represent the surface as many species of vegetation in the scene are heterogeneous in terms of canopy height (Smith et al., 1980; Möller, 2006).

      The salt and pepper impact more observable in the individual and separated class masks than when the classification is whole. Isolated points are likewise easier to spot with highly contrasting colours, and their impact must be acknowledged (Jensen, 2005). If an isolated point appears within another class, the resulting DEM will have a jagged drop at that location. The class masks illustrate the importance of a reliable classification and User's Accuracy as the DEMs build off it directly (Jensen, 2005). If the wrong cover is assigned to a location, the adjustment being made is for the incorrect species of vegetation and further increases error. The class masks are complex to produce, requiring the reclassify tool. One must account for the class value in all raster calculator functions.

Greater RMSE was observed in the first DEM compared to the second. This is not surprising as the first method assumed an entire species of vegetation grew at the same height. On a whole, DEM error was reduced in half by implementing function method. Error reached a maximum of around 60 cm for the first DEM. This error value was constrained by the DSM elevation and the subtraction value used. Error greater than the subtraction value in use is a product of error within the DSM for that location. Error reached maximum of 30 cm in the function subtraction, about half of its counterpart.

Calculating the RMSE per class revealed where the error was coming from in the respective DEMs. RMSE was high for all classes except *S. patens* in the first DEM, while RMSE was low for all classes except *S. patens* in the second DEM. Coupling methods produced the most accurate product, reaching half the RMSE of the function-based method. A final DEM RMSE of 6 cm was determined. This is a desired accuracy as it compares to the RMSE of the DSM in bare earth locations. This reported RMSE merits further studies applying and investigating the capacity of emerging technologies to produce high quality geospatial products.

S. patens and the *J. geradii* Dead are the least dynamic species in terms of canopy height range and change between surveys, while *S. alterniflora* and *J. geradii* alive are both very dynamic (Smith et al., 1980; Möller, 2006). It seems that the more dynamic a species is, the better it is represented with the function method (Medeiros *et al*., 2015). If a species has a relatively homogenous canopy height, it seems better represented with the flat subtraction method.

CHAPTER 6

Conclusion

This project initially set out to answer the question "What combination of parameters for a multispectral equipped UAS will yield the most accurate and useful landcover classifications and DEM for the saltmarsh landscape?". Accuracy was similar across the landcover classifications of varying altitudes, but the DSMs from the flights with lower G.S.D. had higher RMSE values. The 90m RGB and MS flights are regarded as more useful flight altitudes as they were able to cover the entire area of study in a feasible time. For the purposes of this project and generating geospatial products, the 90m multispectral flight seems to strike the greatest balance of accuracy and practicality.

This project has demonstrated the ability of a consumer grade multispectral UAS to produce a suite of geospatial products including reflectance maps, DSMs, land cover classifications, and DEMs with acceptable accuracy (in this study, a DEM with an RMSE of 6cm). Future studies are required to further test and develop the capacity of multispectral sensor equipped UAS to produce accurate geospatial products within the saltmarsh landscape. Further studies investigating alternative methods of land cover classifications such as Object Based Image Analysis and determining the relationships between canopy height and reflectance values would serve to further increase the accuracy of DEMs generated.

The advancements within domains of UASs, multispectral sensors and SFM-MVS software have collectively increased geoscientists' ability to create accurate geospatial products

at a fraction of their previous cost (Colomina and Molina, 2014; Crutsinger *et al*., 2016). As these technologies become cheaper and of higher functionality, it remains ever important to test and push their limits, while scientifically questioning what they claim to do, and how. These further developing technologies, including multispectral UAS, demonstrate promise for researchers and practitioners across a variety of disciplines.

LIST OF REFERENCES

Aber, J. S., Marzolff, I., and Ries, J. B. (2010). *Small-format aerial photography: principles, techniques and geoscience applications*. Amsterdam: Elsevier.

Allen, J. R. (1990). The Formation of Coastal peat marshes under an upward tendency of relative sea-level. *Journal of the Geological Society, 147*(5), 743-745. doi:10.1144/gsjgs.147.5.0743

Amos, C. L. (1995). Siliciclastic tidal flats. Perillo, G. M. (Ed.), *Geomorphology and Sedimentology of Estuarie*. (Ch. 11, pp. 273-306). Amsterdam: Elsevier

Beaumont, N., Jones, L., Garbutt, A., Hansom, J., and Toberman, M. (2013). The value of carbon sequestration and storage in coastal habitats. *Estuarine, Coastal and Shelf Science, 137*, 32-40. doi:10.1016/j.ecss.2013.11.022

Biodiversity Information System for Europe. (2010*). Ecosystem services*. Retrieved November 13, 2017, from https://biodiversity.europa.eu/topics/ecosystem-services

Bleakney, J. (2004). *Sods, Soil, and Spades - The Acadians at Grand Pré and Their Dykeland Legacy*. Montreal: McGill-Queen's University Press.

Carrivick, J. L., Smith, M. W., & Quincey, D. J. (2016*). Structure from motion in the geosciences*. Chichester: Wiley-Blackwell.

Chmura, G. L. (2013). What do we need to assess the sustainability of the tidal salt marsh carbon sink? *Ocean and Coastal Management*, *83,* 25-31. doi:10.1016/j.ocecoaman.2011.09.006

Colomina, I., and Molina, P. (2014). Unmanned aerial systems for photogrammetry and remote sensing: A review. *ISPRS Journal of Photogrammetry and Remote Sensing*, *92*, 79-97. doi:10.1016/j.isprsjprs.2014.02.013

Congalton, (1991). A review of assessing the accuracy of classifications of remotely sensed data. *Remote Sensing of Environment*, *37* (1), 35-46.

Crutsinger, G. M., Short, J., and Sollenberger, R. (2016). The future of UAVs in ecology: an insider perspective from the Silicon Valley drone industry. *Journal of Unmanned Vehicle Systems*, *4*(3), 161-168. doi:10.1139/juvs-2016-0008

Deegan, L. A., Johnson, D. S., Warren, R. S., Peterson, B. J., Fleeger, J. W., Fagherazzi, S., and Wollheim, W. M. (2012). Coastal eutrophication as a driver of salt marsh loss. *Nature*, *490* (7420), 388-392. doi:10.1038/nature11533

Environment Canada. (2012). Recovery Strategy for the Piping Plover (Charadrius melodus melodus) in Canada. *Species at Risk Act Recovery Strategy Series.* Environment Canada, Ottawa.

Eumetrain. (2010). *Spectral signature of an object*. Retrieved from http://www.eumetrain.org/data/3/36/navmenu.php?page=2.4.0

Fox, L., III. (2015). *Essential Earth Imaging for GIS. Redlands*. California: Esri Press.

Geographisches Institut der Universität Bonn. (n.d.). *Radiometric Resolution*. Retrieved February 05, 2017, from http://www.fis.uni-bonn.de/en/recherchetools/infobox/professionals/resolution/radiometric-resolution

Gedan, K. B., Kirwan, M. L., Wolanski, E., Barbier, E. B., & Silliman, B. R. (2011). The present and future role of coastal wetland vegetation in protecting shorelines: Answering recent challenges to the paradigm. *Climatic Change, 106*(1), 7-29. doi:10.1007/s10584-010-0003-7

Giles, P. (2016). Class 6: *Radiometric Resolution; Atmospheric influences; Image enhancement.* Lecture presented in Class 6 of Remote Sensing of the Environment at Saint Mary's University, Halifax.

Government of Canada. (2017). *Estuaries and Saltmarshes* . Retrieved November 13, 2017, from http://www.speciesatrisk.ca/stewardshipguide/index.php?q=content/estuaries-and-salt-marshes

Gonçalves, J. A., & Henriques, R. (2015). UAV photogrammetry for topographic monitoring of coastal areas. *ISPRS Journal of Photogrammetry and Remote Sensing, 104*, 101-111.

Gonzalez-Aguilera, D., and Rodriguez-Gonzalvez, P. (2017). *Drones—An Open Access Journal*. Drones, 1(1), 1. doi:10.3390/drones1010001

Grebby, S., Naden, J., Cunningham, D., & Tansey, K. (2011). Integrating airborne multispectral imagery and airborne LiDAR data for enhanced lithological mapping in vegetated terrain. *Remote Sensing of Environment, 115*(1), 214-226. doi:10.1016/j.rse.2010.08.019

Haas, F., Hilger, L., Neugirg, F., Umstaedter, K., Breitung, C., Fischer, P., ... & Schmidt, J. (2016). Quantification and analysis of geomorphic processes on a recultivated iron ore mine on the Italian island of Elba using long-term ground-based lidar and

photogrammetric SfM data by a UAV. *Natural Hazards and Earth System Sciences*, *16*(5), 1269-1269.

Harris Geospatial. (2013). *Figure 3: Spectral Resolution of Different Sensors* [Digital image]. Retrieved May 4, 2017, from http://www.harrisgeospatial.com/Learn/WhitepapersDetail/TabId/802/ArtMID/2627/ArticleID/13742/Vegetation-Analysis-Using-Vegetation-Indices-in-ENVI.aspx

Hladik, C.; Alber, M. (2012). Accuracy assessment and correction of a LIDAR-derived salt marsh digital elevation model. *Remote Sensing of the Environment 121*, 224–235.

Hogan, S. D., Kelly, M., Stark, B., and Chen, Y. (2017). Unmanned aerial systems for agriculture and natural resources. *California Agriculture, 71*(1), 5-14. doi:10.3733/ca.2017a0002

Hopkinson, C. S., Cai, W., and Hu, X. (2012). Carbon sequestration in wetland dominated coastal systems—a global sink of rapidly diminishing magnitude. *Current Opinion in Environmental Sustainability, 4*(2), 186-194. doi:10.1016/j.cosust.2012.03.005

Horton, R., Cano, E., Bulanon, D., and Fallahi, E. (2017). Peach Flower Monitoring Using Aerial Multispectral Imaging. *J. Imaging*, *3*(1). doi:10.3390/jimaging3010002

Husson, E., Reese, H., and Ecke, F. (2017, March 7). Combining Spectral Data and a DSM from UAS-Images for Improved Classification of Non-Submerged Aquatic Vegetation. *Remote Sensing*, *9*(2); 247. doi:10.3390/rs9030247

International Civil Aviation Organization (2011). Cir 328, Unmanned Aircraft Systems (UAS) (Report CIR328). ISBN 978-92-9231-751-5

Jaud, M., Grasso, F., Le Dantec, N., Verney, R., Delacourt, C., Ammann, J., Grandjean, P. (2016). Potential of UAVs for monitoring mudflat morphodynamics (application to the seine estuary, France). *ISPRS International Journal of Geo-Information, 5*(4), 50.

JCU. (1995). TropWATER - *Tropical Water and Aquatic Ecosystem Research*. Retrieved November 13, 2017, from https://research.jcu.edu.au/tropwater/research-programs/coastal-estuarine-ecology/protection-and-repair-of-australias-saltmarshes/importance-of-saltmarshes

Jensen, J. R. (2005). *Introductory Digital Image Processing: A Remote Sensing Perspective (3rd ed.).* Upper Saddle River, NJ: Pearson.

Kalacska, M., Chmura, G., Lucanus, O., Bérubé, D., and Arroyo-Mora, J. (2017). Structure from motion will revolutionize analyses of tidal wetland landscapes. *Remote Sensing of Environment, 199,* 14-24. doi:10.1016/j.rse.2017.06.023

Kumar, U. (2015, August 05*). Remote sensing platforms and sensors*. Retrieved February 05, 2017, from http://www.slideshare.net/udaykumardevalla/unit2-51304046

Landscape of Grand Pre. (2017). *The Acadians and the Creation of the Dykeland 1680–1755.* Retrieved November 13, 2017, from http://www.landscapeofgrandpre.ca/the-acadians-and-the-creation-of-the-dykeland-1680ndash1755.html

Li, S., Wang, Y., Li, J., & Gao, X. (2015). Multispectral Image Classification Using a New Bayesian Approach with Weighted Markov Random Fields. *Communications in Computer and Information Science Computer Vision,* 168-178. doi:10.1007/978-3-662-48558-3_17

Lillesand, T. M., and Kiefer, R. W. (1987). *Remote sensing and image interpretation (2nd ed.).* New York: J. Wiley.

Lightbody, A. F., and Nepf, H. M. (2006). Prediction of velocity profiles and longitudinal dispersion in salt marsh vegetation. *Limnology and Oceanography*, *51*(1), 218-228. doi:10.4319/lo.2006.51.1.0218

Long, N., Millescamps, B., Guillot, B., Pouget, F., and Bertin, X. (2016). Monitoring the Topography of a Dynamic Tidal Inlet Using UAV Imagery. *Remote Sensing*, *8*(5), 387. doi:10.3390/rs8050387

Lucieer, A., Jong, S. M. D., & Turner, D. (2014). Mapping landslide displacements using Structure from Motion (SfM) and image correlation of multi-temporal UAV photography. *Progress in Physical Geography*, *38*(1), 97-116. doi:10.1177/0309133313515293

Macreadie, P., Baird, M., Trevathan-Tackett, S., Larkum, A., and Ralph, P. (2014). Quantifying and modelling the carbon sequestration capacity of seagrass meadows – A critical assessment. *Marine Pollution Bulletin, 83*(2), 430-439. doi:10.1016/j.marpolbul.2013.07.038

Medeiros, S., Hagen, S., Weishampel, J., and Angelo, J. (2015). Adjusting Lidar-Derived Digital Terrain Models in Coastal Marshes Based on Estimated Aboveground Biomass Density. *Remote Sensing*, *7*(4), 3507-3525. doi:10.3390/rs70403507

MicaSense. (2017*). What is NDRE?* Retrieved November 13, 2017, from https://www.micasense.com/what-is-ndre/

Moore, D. S., Notz, W. I, & Flinger, M. A. (2013). *The basic practice of statistics (6th ed.).* New York, NY: W. H. Freeman and Company.

Möller, I. (2006). Quantifying saltmarsh vegetation and its effect on wave height dissipation: Results from a UK East coast saltmarsh. *Estuarine, Coastal and Shelf Science, 69*(3-4), 337-351. doi:10.1016/j.ecss.2006.05.003

Maritime Provinces Spatial Analysis Research Centre (MP_SPaRC), Baker, G. (2017, May, 7). *Flight Planning* [Personal communication].

Matheson, G. (2017, March 2). *Site Consultation* [Personal communication].

National Oceanic and Atmospheric Administration. (2008, October 08). *Where is the highest tide?* Retrieved November 13, 2017, from https://oceanservice.noaa.gov/facts/highesttide.html

NRCAN. (2013, November 18). *Image Classification and Analysis*. Retrieved April 05, 2017, from http://www.nrcan.gc.ca/node/9361

Obregon, R. (2009). *Table 4. Current and proposed sensor systems for identifying and mapping urban features.* Retrieved from https://spacejournal.ohio.edu/issue14/images/remote_table4.gif

Parrot. (2016). *Sequoia Official Documentation and Specifications 2016*. Paris, France: Parrot.

Peacock, R. (2014). *Accuracy Assessment of Supervised and Unsupervised Classification using Landsat Imagery of Little Rock, Arkansas: A Thesis Presented to the Department of Humanities and Social Sciences in Candidacy for the Degree of Master of Science (Master's thesis, North West Missouri State University, 2014)*. Maryville: North West Missouri State University.

Pendle, M., and Wallingford, H. (2013*). Estuarine and coastal managed realignment sites in England*. Retrieved November 13, 2017, from http://eprints.hrwallingford.co.uk/664/1/HRPP627-Managed_realignment.pdf

Quintana-Alcantara, Carlos Eduardo. (2014)."*Carbon Sequestration in Tidal Saltmarshes and Mangrove Ecosystems*" Master's Projects. Paper 19.

Rinaldo, A., Belluco, E., Dalpaos, A., Feola, A., Lanzoni, S., & Marani, M. (2004). Tidal Networks: Form and Function. *Coastal and Estuarine Studies*, 75-91. doi:10.1029/ce059p0075

Roberts, B. A., and Robertson, A. (1986). Saltmarshes of Atlantic Canada: their ecology and distribution. *Canadian Journal of Botany, 64*(2), 455-467. doi:10.1139/b86-060

Roe, B. (2016, June 16). *Introduction to Multivariate Classification Problems*. Retrieved April 5, 2017, from https://www.birs.ca/workshops/2006/06w5054/files/byron-roe.pdfhttps://www.birs.ca/workshops/2006/06w5054/files/byron-roe.pdf

Rosenfield, G., Fitzpatrick-Lins, K. (1986). A coefficient of agreement as a measure of thematic classification accuracy. *Photogrammetric Engineering and Remote Sensing, 52*(2). 223-227.

Smith, D.L., Bird, C.J., Lynch, K.D., & McLachlan, J. (1980). Angiosperm productivity in two saltmarshes of Minas Basin. *Proceedings of the Nova Scotian Institute of Science*, *30*(1), 109-118.

Sousa, A. I., Lillebø, A. I., Pardal, M. A., and Caçador, I. (2010). Productivity and nutrient cycling in Saltmarshes: Contribution to ecosystem health. *Estuarine, Coastal and Shelf Science, 87*(4), 640-646. doi:10.1016/j.ecss.2010.03.007

Sousa, L. P., Sousa, A. I., Alves, F. L., and Lillebø, A. I. (2016). Ecosystem services provided by a complex coastal region: challenges of classification and mapping. *Scientific Reports, 6*(1). doi:10.1038/srep22782

Spring, K., Flynn, B., Long, J., and Davidson, M. (2016). *Spatial Resolution in Digital Imaging*. Retrieved February 05, 2017, from https://www.microscopyu.com/tutorials/spatial-resolution-in-digital-imaging

Spiral Commercial Services. (2015). *NDRE*, Retrieved November 13, 2017, from http://aerialagimagery.com/NDRE.html

Statistics Solutions. (2018). *Sample Size Formula*. Retrieved April 10, 2018, from http://www.statisticssolutions.com/sample-size-formula/

Story, M. and Congalton, R.G. (1986). Accuracy Assessment: A User's Perspective. *Photogrammetric Engineering and Remote Sensing*, *52*, 397-399.

Sturari, M., Frontoni, E., Pierdicca, R., Mancini, A., Malinverni, S., Tassetti, A., and Zingaretti, P. (2017). Integrating elevation data and multispectral high resolution images for an improved hybrid Land Use/Land Cover mapping. *European Journal of Remote Sensing, 50*(1), 1-17. doi:10.1080/22797254.2017.1274572

UK Marine. (2001). *Advantages and Disadvantages of Remote Sampling Techniques for the Sea Pens and Burrowing Megafauna Biotope Complex*. Retrieved April 05, 2017, from http://www.ukmarinesac.org.uk/communities/seapens/sp6_1_1.htm

UMaine. (2017). *Vegetation Zones.* Retrieved November 13, 2017, from http://www.seagrant.umaine.edu/coastal-hazards-guide/coastal-wetlands/learn-more/vegetation-zones

USGS/NPS . (1994). Field Methods for Vegetation Mapping. *USGS/NPS Vegetation Mapping Program*, 1-112. Retrieved from https://www1.usgs.gov/vip/standards/fieldmethodsrpt.pdf.

Westoby, M. J., Brasington, J., Glasser, N. F., Hambrey, M. J., & Reynolds, J. M. (2012). 'Structure-from-Motion' photogrammetry: A low-cost, effective tool for geoscience applications. *Geomorphology, 179*, 300-314.

Wiegert, R. G., Pomeroy, L. R., and Wiebe, W. J. (1981). Ecology of Saltmarshes: An Introduction. *Ecological Studies*, 3-19. doi:10.1007/978-1-4612-5893-3_1

Wu, M., Yang, C., Song, X., Hoffman, W., Huang, W., Niu, Z., Li, W. (2017). *Evaluation of Orthomosics and Digital Surface Models Derived from Aerial Imagery for Crop Type Mapping*. Retrieved April 5, 2017, from http://www.mdpi.com/2072-4292/9/3/239/htm doi: 10.3390/rs9030239

Yengoh, G. T., Dent, D., Olsson, L., Tengberg, A. E., and J., T. I. (2015). *Use of the Normalized Difference Vegetation Index (NDVI) to Assess Land Degradation at Multiple Scales Current Status, Future Trends, and Practical Considerations*. Cham: Springer International Publishing.

Zottoli, R. (2015, April 14). *Spartina patens (Zone 3).* Retrieved from https://zottoli.wordpress.com/saltmarshes/spartina-patens-zone-3/.

APPENDIX

Monoculture Surveys *S. alterniflora*

Cover Alt	Cell A	Survey 1	RNG Sample# 7	Cover Alternaflora	Cell A	Survey 2	RNG Sample# 15
Veg Grid #	Hit	Cover %	Veg Height	Veg Grid #	Hit	Cover %	Veg Height
1	Y	25	35	1	Y	25	28
2	Y	0		2	Y	75	
3	Y	25		3	Y	5	
4	Y	25		4	Y	5	
5	Y	25	30	5	Y	50	50
6	Y	25		6	Y	5	
7	Y	25		7	Y	25	
8	Y	50		8	Y	25	
9	Y	25		9	Y	75	
10	Y	25		10	Y	25	
11	Y	50		11	N	75	
12	Y	50		12	Y	50	
13	Y	50	50	13	Y	50	48
14	Y	25		14	Y	75	
15	Y	25		15	N	50	
16	Y	75		16	N	75	
17	Y	75		17	Y	50	
18	Y	50		18	Y	25	
19	Y	50		19	Y	50	
20	Y	50	45	20	Y	25	48
21	Y	50		21	Y	25	
22	Y	75		22	Y	50	
23	Y	75		23	Y	50	
24	Y	75		24	Y	25	
25	Y	25	20	25	Y	50	71
Canopy Height 50cm				Canopy Height 53cm			
Alternaflora Cell A Survey 3 RNG Sample 14				Canopy Height 59cm			
1	Y	25	55	13	Y	50	64
2	N	50		14	Y	25	
3	Y	75		15	Y	50	
4	Y	50		16	Y	50	
5	N	25	36	17	Y	25	
6	Y	25		18	Y	25	
7	Y	25		19	Y	25	
8	Y	25		20	Y	5	61
9	Y	25		21	Y	5	
10	Y	5		22	Y	25	
11	Y	50		23	Y	25	
12	Y	50		24	Y	75	
Waypoint 2				25	Y	75	50

Table A.1: S. alterniflora vegetation survey, Cell A

Monoculture Surveys *S. alterniflora*

Cover Alternaflora	Cell C	Survey 1	RNG Sample# 13	Cover Alternaflora	Cell C	Survey 2	RNG Sample# 16
Veg Grid #	Hit	Cover %	Veg Height	Veg Grid #	Hit	Cover %	Veg Height
1	Y	75	45	1	Y	50	55
2	Y	50		2	Y	50	
3	Y	75		3	Y	75	
4	Y	75		4	Y	75	
5	Y	25	45	5	Y	75	45
6	Y	25		6	Y	25	
7	Y	75		7	Y	25	
8	Y	75		8	Y	25	
9	Y	75		9	N	50	
10	Y	100		10	Y	50	
11	Y	50		11	Y	50	
12	Y	75		12	Y	50	
13	Y	75	47	13	Y	75	50
14	Y	25		14	Y	75	
15	Y	25		15	Y	50	
16	Y	75		16	Y	25	
17	Y	25		17	Y	50	
18	Y	50		18	Y	75	
19	Y	50		19	Y	75	
20	Y	50	58	20	Y	50	55
21	Y	50		21	Y	25	
22	Y	25		22	Y	50	
23	Y	25		23	Y	25	
24	Y	25		24	Y	25	
25	Y	25	45	25	Y	75	45
Canopy Height 60				Canopy Height 60			

Alternaflora	Cell C	Survey 3	RNG Sample 9	Canopy Height 65			
1	Y	50	50	13	Y	50	55
2	Y	100		14	Y	25	
3	Y	50		15	Y	25	
4	Y	50		16	Y	50	
5	Y	75	60	17	Y	75	
6	Y	25		18	Y	50	
7	Y	50		19	Y	25	
8	Y	75		20	Y	75	50
9	Y	75		21	Y	100	
10	Y	75		22	Y	75	
11	Y	50		23	Y	50	
12	Y	75		24	Y	25	
Waypoint 17				25	Y	75	60

Table A.2: S. alterniflora vegetation survey, Cell C

Monoculture Surveys *S. alterniflora*

Cover Alternaflora	Cell B	Survey 1	RNG Sample# 6	Cover Alternaflora	Cell B	Survey 2	RNG Sample# 12
Veg Grid #	Hit	Cover %	Veg Height	Veg Grid #	Hit	Cover %	Veg Height
1	Y	100	53	1	Y	75	60
2	Y	100		2	Y	90	
3	Y	100		3	N	90	
4	Y	100		4	Y	75	
5	Y	100	118	5	Y	50	44
6	Y	100		6	Y	75	
7	Y	100		7	Y	100	
8	Y	100		8	Y	90	
9	Y	100		9	Y	75	
10	Y	100		10	Y	50	
11	Y	100		11	Y	50	
12	Y	100		12	Y	90	
13	Y	100	101	13	N	25	57
14	Y	100		14	Y	25	
15	Y	100		15	Y	25	
16	Y	100		16	Y	50	
17	Y	100		17	Y	50	
18	Y	100		18	Y	50	
19	Y	100		19	Y	25	
20	Y	100	91	20	Y	25	62
21	Y	75		21	Y	50	
22	Y	75		22	Y	25	
23	Y	100		23	Y	50	
24	Y	100		24	Y	25	
25	Y	100	103	25	Y	25	101
Canopy Height 102				Canopy Height 88			
Alternaflora	Cell B	Survey 3	RNG Sample 5	Canopy height 89			
1	Y	90	90	13	Y	75	105
2	Y	90		14	Y	100	
3	Y	100		15	Y	100	
4	Y	90		16	Y	75	
5	Y	90	110	17	Y	100	
6	Y	100		18	Y	90	
7	Y	100		19	Y	50	
8	Y	100		20	Y	75	96
9	Y	100		21	Y	100	
10	Y	100		22	Y	75	
11	Y	90		23	Y	100	
12	Y	100		24	Y	75	
Waypoint 13				25	Y	100	72

Table A.3: S. alterniflora vegetation survey, Cell B

Monoculture Surveys *S. patens*

Cover Patens	Cell A	Survey 1	RNG Sample# 6	Cover Patens	Cell A	Survey 2	RNG Sample# 2
Veg Grid #	Hit	Cover %	Veg Height	Veg Grid #	Hit	Cover %	Veg Height
1	Y	100	35	1	Y	100	50
2	Y	100		2	Y	100	
3	Y	100		3	Y	100	
4	Y	100		4	Y	100	
5	Y	100	35	5	Y	100	55
6	Y	100		6	Y	100	
7	Y	100		7	Y	100	
8	Y	100		8	Y	100	
9	Y	100		9	Y	100	
10	Y	100		10	Y	100	
11	Y	100		11	Y	100	
12	Y	100		12	Y	100	
13	Y	100	45	13	Y	100	46
14	Y	100		14	Y	100	
15	Y	100		15	Y	100	
16	Y	100		16	Y	100	
17	Y	100		17	Y	100	
18	Y	100		18	Y	100	
19	Y	100		19	Y	100	
20	Y	100	50	20	Y	100	38
21	Y	100		21	Y	100	
22	Y	100		22	Y	100	
23	Y	100		23	Y	100	
24	Y	100		24	Y	100	
25	Y	100	43	25	Y	100	46
Canopy Height 9cm				Canopy Height 9cm			
Patens	Cell A	Survey 3	RNG Sample 4	Canopy Height 10cm			
1	Y	100	43	13	Y	100	56
2	Y	100		14	Y	100	
3	Y	100		15	Y	100	
4	Y	100		16	Y	100	
5	Y	100	71	17	Y	100	
6	Y	100		18	Y	100	
7	Y	100		19	Y	100	
8	Y	100		20	Y	100	46
9	Y	100		21	Y	100	
10	Y	100		22	Y	100	
11	Y	100		23	Y	100	
12	Y	100		24	Y	100	
Waypoint 3				25	Y	100	46

Table A.4: S. patens vegetation survey, Cell A

Monoculture Surveys *S. patens*

Cover Patens	Cell C	Survey 1	RNG Sample# 15	Cover Patens	Cell C	Survey 2	RNG Sample# 9
Veg Grid #	Hit	Cover %	Veg Height	Veg Grid #	Hit	Cover %	Veg Height
1	Y	100	30	1	Y	100	40
2	Y	100		2	Y	100	
3	Y	100		3	Y	100	
4	Y	100		4	Y	100	
5	Y	100	35	5	Y	100	38
6	Y	100		6	Y	100	
7	Y	100		7	Y	100	
8	Y	100		8	Y	100	
9	Y	100		9	N	100	
10	Y	100		10	Y	100	
11	Y	100		11	Y	100	
12	Y	100		12	Y	100	
13	Y	100	30	13	Y	100	40
14	Y	100		14	Y	100	
15	Y	100		15	Y	100	
16	Y	100		16	Y	100	
17	Y	100		17	Y	100	
18	Y	100		18	Y	100	
19	Y	100		19	Y	100	
20	Y	100	38	20	Y	100	45
21	Y	100		21	Y	100	
22	Y	100		22	Y	100	
23	Y	100		23	Y	100	
24	Y	100		24	Y	100	
25	Y	100	35	25	Y	100	40
Canopy Height 8cm				Canopy Height 10cm			
Patens	Cell C	Survey 3	RNG Sample 16	Canopy Height 7cm			
1	Y	100	35	13	Y	100	30
2	Y	100		14	Y	100	
3	Y	100		15	Y	100	
4	Y	100		16	Y	100	
5	Y	100	30	17	Y	100	
6	Y	100		18	Y	100	
7	Y	100		19	Y	100	
8	Y	100		20	Y	100	35
9	Y	100		21	Y	100	
10	Y	100		22	Y	100	
11	Y	100		23	Y	100	
12	Y	100		24	Y	100	
Waypoint 17				25	Y	100	40

Table A.5: S. patens vegetation survey, Cell C

Monoculture Surveys *S. patens*

Cover Patens	Cell B	Survey 1	RNG Sample# 1	Cover Patens	Cell B	Survey 2	RNG Sample# 7
Veg Grid #	Hit	Cover %	Veg Height	Veg Grid #	Hit	Cover %	Veg Height
1	Y	100	50	1	Y	100	52
2	Y	100		2	Y	100	
3	Y	100		3	N	100	
4	Y	100		4	Y	100	
5	Y	100	62	5	Y	100	48
6	Y	100		6	Y	100	
7	Y	100		7	Y	100	
8	Y	100		8	Y	100	
9	Y	100		9	Y	100	
10	Y	100		10	Y	100	
11	Y	100		11	Y	100	
12	Y	100		12	Y	100	
13	Y	100	67	13	N	100	47
14	Y	100		14	Y	100	
15	Y	100		15	Y	100	
16	Y	100		16	Y	100	
17	Y	100		17	Y	100	
18	Y	100		18	Y	100	
19	Y	100		19	Y	100	
20	Y	100	77	20	Y	100	53
21	Y	100		21	Y	100	
22	Y	100		22	Y	100	
23	Y	100		23	Y	100	
24	Y	100		24	Y	100	
25	Y	100	47	25	Y	100	49
Canopy Height 7 cm				Canopy Height 8cm			

Patens	Cell B	Survey 3	RNG Sample 14	Canopy height 8cm			
1	Y	100	56	13	Y	100	50
2	Y	100		14	Y	100	
3	Y	100		15	Y	100	
4	Y	100		16	Y	100	
5	Y	100	53	17	Y	100	
6	Y	100		18	Y	100	
7	Y	100		19	Y	100	
8	Y	100		20	Y	100	56
9	Y	100		21	Y	100	
10	Y	100		22	Y	100	
11	Y	100		23	Y	100	
12	Y	100		24	Y	100	
Waypoint 14				25	Y	100	47

Table A.6: S. patens vegetation survey, Cell B

Monoculture Surveys *J. geradii* alive

Cover	Cell	Survey	RNG	Cover	Cell	Survey	RNG Sample#
Ger Alive	A	1	6	Patens	A	2	15
Veg Grid #	Hit	Cover %	Veg Height	Veg Grid #	Hit	Cover %	Veg Height
1	Y	100	47	1	Y	100	44
2	Y	100		2	Y	100	
3	Y	100		3	Y	100	
4	Y	100		4	Y	100	
5	Y	100	50	5	Y	100	48
6	Y	100		6	Y	100	
7	Y	100		7	Y	100	
8	Y	100		8	Y	100	
9	Y	100		9	Y	100	
10	Y	100		10	Y	100	
11	Y	100		11	Y	100	
12	Y	100		12	Y	100	
13	Y	100	36	13	Y	100	56
14	Y	100		14	Y	100	
15	Y	100		15	Y	100	
16	Y	100		16	Y	100	
17	Y	100		17	Y	100	
18	Y	100		18	Y	100	
19	Y	100		19	Y	100	
20	Y	100	35	20	Y	100	44
21	Y	100		21	Y	100	
22	Y	100		22	Y	100	
23	Y	100		23	Y	100	
24	Y	100		24	Y	100	
25	Y	100	35	25	Y	100	38
Canopy Height 36 cm				Canopy Height 37 cm			
Patens	Cell A	Survey 3	RNG Sample 1	Canopy Height 36 cm			
1	Y	100	43	13	Y	100	43
2	Y	100		14	Y	100	
3	Y	100		15	Y	100	
4	Y	100		16	Y	100	
5	Y	100	45	17	Y	100	
6	Y	100		18	Y	100	
7	Y	100		19	Y	100	
8	Y	100		20	Y	100	44
9	Y	100		21	Y	100	
10	Y	100		22	Y	100	
11	Y	100		23	Y	100	
12	Y	100		24	Y	100	
Waypoint 5				25	Y	100	42

Table A.7: G. geradii alive vegetation survey, Cell A

Monoculture Surveys *J. geradii* alive

Cover Patens Veg Grid	Cell B Hit	Survey 1 Cover %	RNG 2 Other Hits	Veg Height	Cover Patens Veg Grid #	Cell B Hit	Survey 2 Cover %	RNG 8 Other Hits	Veg Height
1	Y	100		40	1	Y	100		40
2	Y	100			2	Y	100		
3	Y	75	Gold		3	N	100		
4	Y	75	Gold		4	Y	100		
5	Y	100		35	5	Y	100		35
6	Y	100			6	Y	100		
7	Y	100			7	Y	100	Arrow	
8	Y	75			8	Y	100	Arrow	
9	Y	100	Gold		9	Y	100	Arrow	
10	Y	100			10	Y	100		
11	Y	75			11	Y	100		
12	Y	75			12	Y	100		
13	Y	100		40	13	N	100	Arrow	40
14	Y	100			14	Y	100	Arrow	
15	Y	100			15	Y	100	Arrow	
16	Y	100			16	Y	100		
17	Y	75			17	Y	100		
18	Y	100	Gold, Arrow		18	Y	100	Arrow	
19	Y	100	Gold		19	Y	100		
20	Y	100		35	20	Y	100	Arrow	30
21	Y	100	Gold		21	Y	100		
22	Y	100	Gold		22	Y	100	Milk	
23	Y	100			23	Y	100		
24	Y	100			24	Y	100		
25	Y	100		35	25	Y	100		35
Canopy Height 38 cm					Canopy Height 36 cm				

Patens	Cell B	Survey 3	RNG Sample 11		Canopy height 34 cm				
1	Y	100		33	13	Y	100		40
2	Y	100	Arrow		14	Y	100		
3	Y	100			15	Y	100		
4	Y	100			16	Y	100		
5	Y	100		35	17	Y	100		
6	Y	100	Arrow		18	Y	100		
7	Y	100	Arrow		19	Y	100		
8	Y	100			20	Y	100		35
9	Y	100			21	Y	100		
10	Y	100			22	Y	75		
11	Y	100			23	Y	75	Rack	
12	Y	100			24	Y	100		
Waypoint 15					25	Y	100		34

Table A.8: G. geradii alive vegetation survey, Cell C

Monoculture Surveys *J. geradii* alive

Cover Patens Veg Grid	Cell C Hit	Survey 1 Cover %	RNG 1 Other Hits	RNG 1 Veg Height	Cover Patens Veg Grid #	Cell C Hit	Survey 2 Cover %	RNG 7 Other Hits	RNG 7 Veg Height
1	Y	100		35	1	Y	100		40
2	Y	100			2	Y	100		
3	Y	100	Milk		3	Y	100		
4	Y	100			4	Y	100		
5	Y	100		35	5	Y	100		40
6	Y	100			6	Y	100		
7	Y	100			7	Y	100		
8	Y	100			8	Y	100		
9	Y	100			9	Y	100	GT	
10	Y	100			10	Y	100	GT	
11	Y	100			11	Y	100		
12	Y	100	Milk		12	Y	100	GT	
13	Y	100		35	13	Y	100	Milk	40
14	Y	100			14	Y	100		
15	Y	100			15	Y	100		
16	Y	100			16	Y	100		
17	Y	100			17	Y	100	Milk	
18	Y	100			18	Y	100		
19	Y	100			19	Y	100		
20	Y	100		40	20	Y	100		40
21	Y	100			21	Y	100		
22	Y	100			22	Y	100		
23	Y	100	Milk		23	Y	100		
24	Y	100			24	Y	100		
25	Y	100		35	25	Y	100		35
Canopy Height 35 cm					Canopy Height 40 cm				

Patens	Cell C	Survey 3	RNG Sample 16				Canopy height 35 cm		
1	Y	100		35	13	Y	100		35
2	Y	100			14	Y	100		
3	Y	100	GT		15	Y	100		
4	Y	100	GT		16	Y	100	GT	
5	Y	100		35	17	Y	100	GT	
6	Y	100			18	Y	100	GT	
7	Y	100			19	Y	100	GT	
8	Y	100	GT		20	Y	100		30
9	Y	100	GT		21	Y	100	GT	
10	Y	100	GT		22	Y	75		
11	Y	100			23	Y	75	MIlk	
12	Y	100			24	Y	100	GT	
Waypoint 15					25	Y	100	Milk	35

Table A.9: G. geradii alive vegetation survey, Cell B

Monoculture Surveys *J. geradii dying*

Cover Ger Dying	Cell A	Survey 1	RNG 10	Cover Ger Dying	Cell A	Survey 2	RNG Sample# 5
Veg Grid #	Hit	Cover %	Veg Height	Veg Grid #	Hit	Cover %	Veg Height
1	Y	100	61	1	Y	100	50
2	Y	100		2	Y	100	
3	Y	100		3	Y	100	
4	Y	100		4	Y	100	
5	Y	100	51	5	Y	100	75
6	Y	100		6	Y	100	
7	Y	100		7	Y	100	
8	Y	100		8	Y	100	
9	Y	100		9	Y	100	
10	Y	100		10	Y	100	
11	Y	100		11	Y	100	
12	Y	100		12	Y	100	
13	Y	100	50	13	Y	100	48
14	Y	100		14	Y	100	
15	Y	100		15	Y	100	
16	Y	100		16	Y	100	
17	Y	100		17	Y	100	
18	Y	100		18	Y	100	
19	Y	100		19	Y	100	
20	Y	100	51	20	Y	100	55
21	Y	100		21	Y	100	
22	Y	100		22	Y	100	
23	Y	100		23	Y	100	
24	Y	100		24	Y	100	
25	Y	100	47	25	Y	100	50
Canopy Height 6 cm				Canopy Height 7 cm			

Ger Dying	Cell A	Survey 3	RNG Sample 9	Canopy Height 6 cm			
1	Y	100	50	13	Y	100	59
2	Y	100		14	Y	100	
3	Y	100		15	Y	100	
4	Y	100		16	Y	100	
5	Y	100	52	17	Y	100	
6	Y	100		18	Y	100	
7	Y	100		19	Y	100	
8	Y	100		20	Y	100	51
9	Y	100		21	Y	100	
10	Y	100		22	Y	100	
11	Y	100		23	Y	100	
12	Y	100		24	Y	100	
Waypoint 5				25	Y	100	48

Table A.10: G. geradii dead vegetation survey, Cell A

Monoculture Surveys *J. geradii dying*

Cover Ger/ Pat	Cell B	Survey 1	RNG 5		Cover Ger/ Pat	Cell B	Survey 2	RNG 8	
Veg Grid #	Hit	Cover %	Other Hits	Veg Heig	Veg Grid #	Hit	Cover %	Other Hits	Veg Heig
1	Y,Y	100		40	1	Y,Y	100	Arrow	40
2	Y,Y	100	GT		2	Y,Y	100	Arrow, Milk	
3	Y,Y	100			3	Y,Y	100	Arrow, Milk	
4	Y,Y	100			4	Y,Y	100	Arrow, Milk	
5	Y,Y	100		37	5	Y,Y	100	Arrow, Milk	38
6	Y,Y	100			6	Y,Y	100	Arrow, Milk	
7	Y,Y	100			7	Y,Y	100	Arrow, Milk	
8	Y,Y	100	GT		8	Y,Y	100	Arrow, Milk	
9	Y,Y	100	GT		9	Y,Y	100	Arrow, Milk	
10	Y,Y	100	GT		10	Y,Y	100	Arrow, Milk	
11	Y,Y	100			11	Y,Y	100		
12	Y,Y	100			12	Y,Y	100		
13	Y,Y	100	Pat dom.	40	13	Y,Y	100	Arrow	40
14	Y,Y	100			14	Y,Y	100	Arrow	
15	Y,Y	100			15	Y,Y	75	Arrow,	
16	Y,Y	100			16	Y,Y	100		
17	Y,Y	100			17	Y,Y	100		
18	Y,Y	100			18	Y,Y	100	Arrow	
19	Y,Y	100			19	Y,Y	100		
20	Y,Y	100		37	20	Y,Y	100	Arrow	37
21	Y,Y	100			21	Y,Y	100		
22	Y,Y	100			22	Y,Y	100	Milk	
23	Y,Y	100			23	Y,Y	100		
24	Y,Y	100			24	Y,Y	100		
25	Y,Y	100		40	25	Y,Y	100		32
Canopy Height 9 cm					Canopy Height 9 cm				

Ger/Pat	Cell B	Survey 3	RNG Sample 13		Canopy height 8 cm				
1	Y, Y	100		40	13	Y, Y	100		40
2	Y, Y	100			14	Y, N	100	Arrow	
3	Y, N	100			15	Y, Y	100		
4	Y, N	100			16	Y, Y	100		
5	Y, Y	100		35	17	Y, Y	100		
6	Y, N	100			18	Y, Y	100		
7	Y, Y	100			19	Y, N	100		
8	Y, N	100			20	Y, Y	100		35
9	Y, Y	100			21	Y, Y	100		
10	Y, Y	100			22	Y, Y	75		
11	Y, Y	100			23	Y, Y	75		
12	Y, Y	100			24	Y, Y	100		
Waypoint 16					25	Y, Y	100		40

Table A.11: G. geradii dead vegetation survey, Cell C

Monoculture Surveys *J. geradii dying*

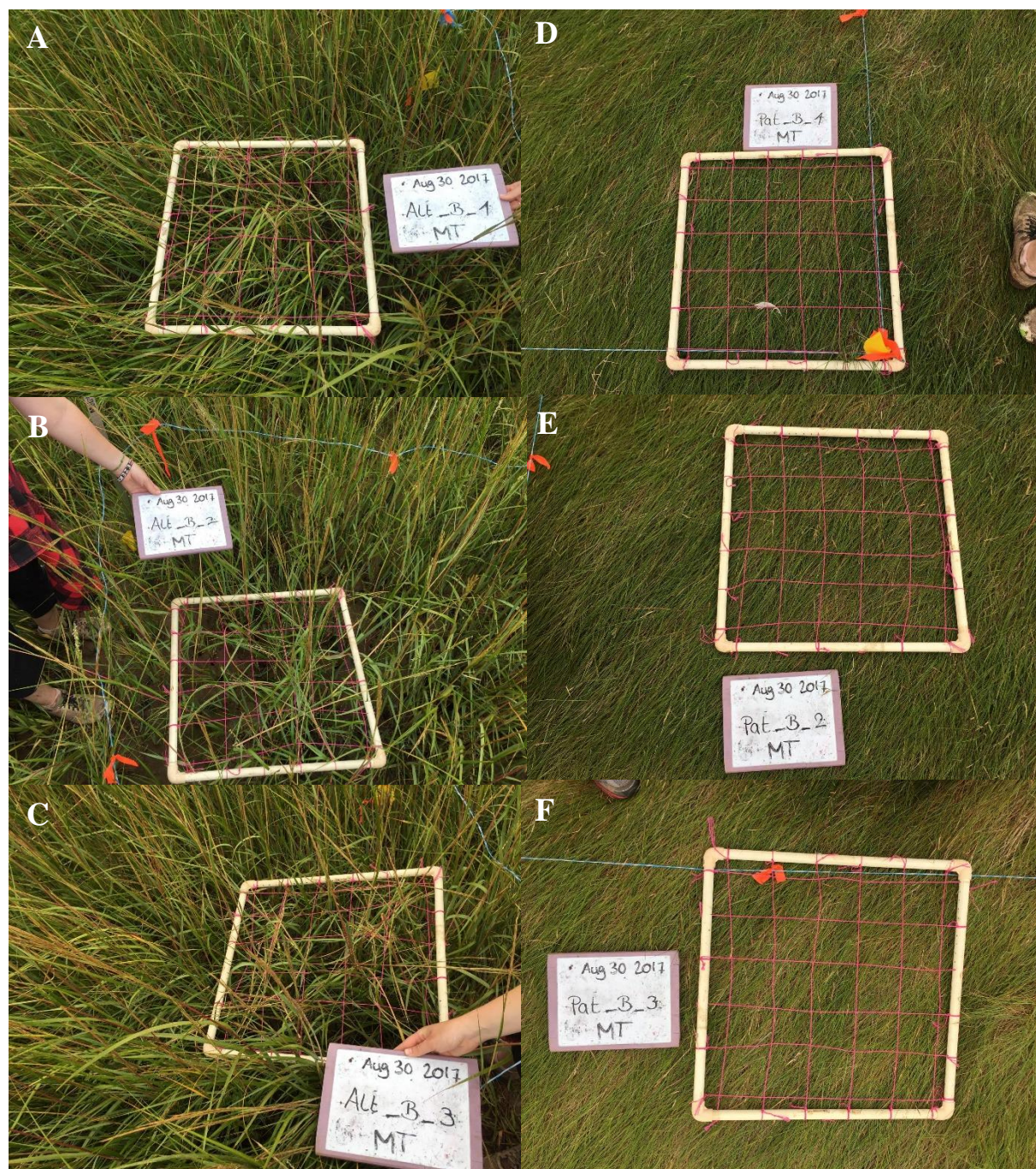| Cover Ger Dying Veg Grid #	Cell C Hit	Survey 1 Cover %	RNG 1 Other Hits	Veg Height	Cover Ger Dying Veg Grid #	Cell C Hit	Survey 2 Cover %	RNG 7 Other Hits	Veg Height
1	Y	100		35	1	Y	100		40
2	Y	100			2	Y	100		
3	Y	100	Milk		3	Y	100		
4	Y	100			4	Y	100		
5	Y	100		35	5	Y	100		40
6	Y	100			6	Y	100		
7	Y	100			7	Y	100		
8	Y	100			8	Y	100		
9	Y	100			9	Y	100	GT	
10	Y	100			10	Y	100	GT	
11	Y	100			11	Y	100		
12	Y	100	Milk		12	Y	100	GT	
13	Y	100		35	13	Y	100	Milk	40
14	Y	100			14	Y	100		
15	Y	100			15	Y	100		
16	Y	100			16	Y	100		
17	Y	100			17	Y	100	Milk	
18	Y	100			18	Y	100		
19	Y	100			19	Y	100		
20	Y	100		40	20	Y	100		40
21	Y	100			21	Y	100		
22	Y	100			22	Y	100		
23	Y	100	Milk		23	Y	100		
24	Y	100			24	Y	100		
25	Y	100		35	25	Y	100		35
Canopy Height 35 cm					Canopy Height 40 cm				
Ger Dying	Cell C	Survey 3	RNG Sample 16		Canopy height 35 cm				
1	Y	100		35	13	Y	100		35
2	Y	100			14	Y	100		
3	Y	100	GT		15	Y	100		
4	Y	100	GT		16	Y	100	GT	
5	Y	100		35	17	Y	100	GT	
6	Y	100			18	Y	100	GT	
7	Y	100			19	Y	100	GT	
8	Y	100	GT		20	Y	100		30
9	Y	100	GT		21	Y	100	GT	
10	Y	100	GT		22	Y	75		
11	Y	100			23	Y	75	Mllk	
12	Y	100			24	Y	100	GT	
Waypoint 15					25	Y	100	Milk	35

Table A.12: G. geradii dead vegetation survey, Cell B

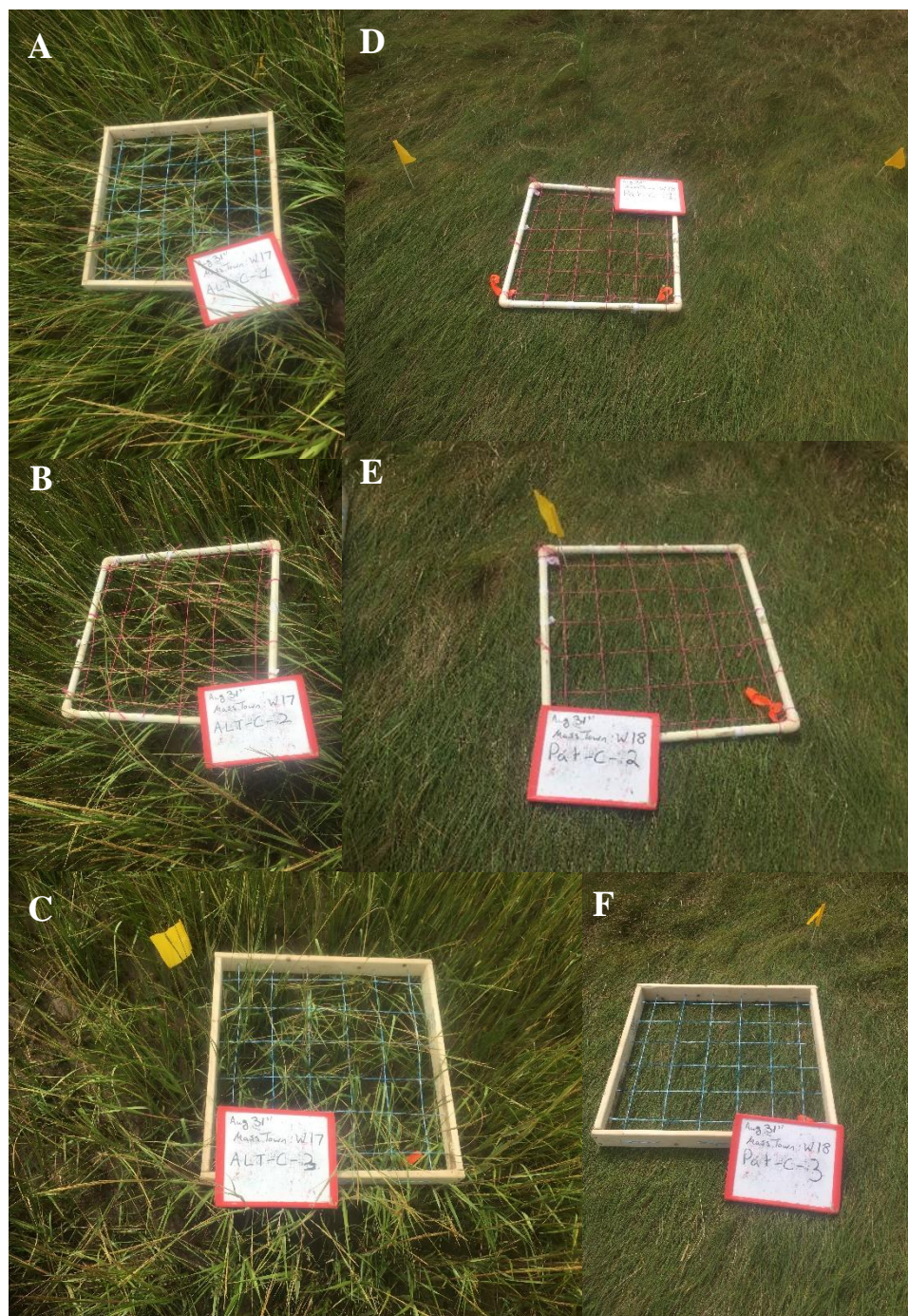*Figure A.13 (A-F): Cell B S. alterniflora (A-C) and S. patens (D-F) survey images*

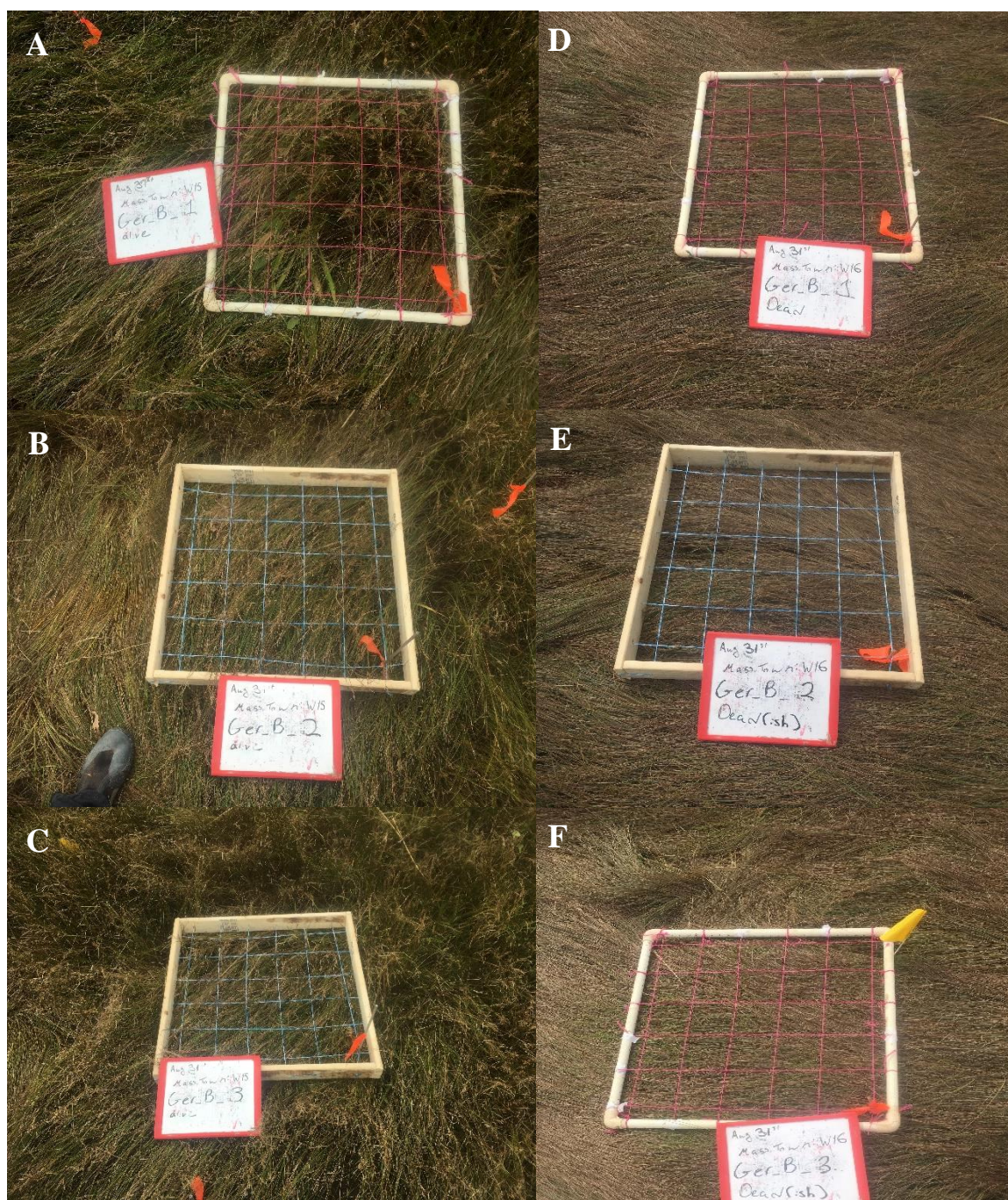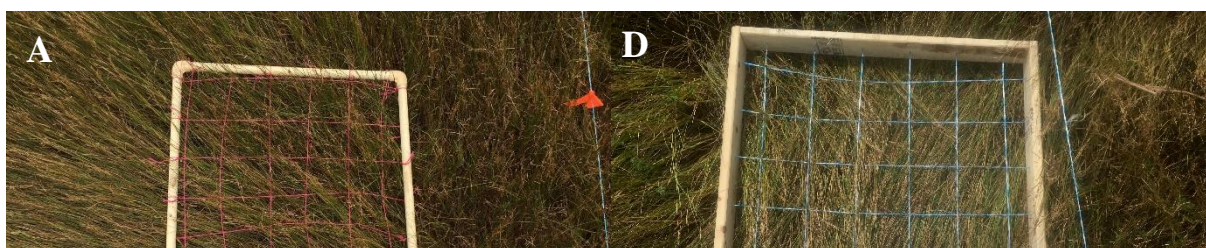*Figure A.14 (A-F): Cell C S. alterniflora (A-C) and S. patens (D-F) survey images*

Figure A.15 (A-F): Cell B J. geradii alive (A-C) and dead (D-F) survey images

Summary

Project	MTE_MS_50m
Processed	2017-09-27 17:58:23
Camera Model Name(s)	Sequoia_4.0_1280x960 (Green), Sequoia_4.0_1280x960 (Red), Sequoia_4.0_1280x960 (Red edge), Sequoia_4.0_1280x960 (NIR)
Rig name(s)	«Sequoia»
Average Ground Sampling Distance (GSD)	5.26 cm / 2.07 in
Area Covered	0.0736 km^2 / 7.3593 ha / 0.0284 sq. mi. / 18.1947 acres

Quality Check

Images	median of 11872 keypoints per image	✓
Dataset	2484 out of 2496 images calibrated (99%), all images enabled	✓
Camera Optimization	0.05% relative difference between initial and optimized internal camera parameters	✓
Matching	median of 5698.87 matches per calibrated image	✓
Georeferencing	yes, 8 GCPs (8 3D), mean RMS error = 0.016 m	✓

Summary

Project	MTE_MS_70M
Processed	2017-09-27 09:15:35
Camera Model Name(s)	Sequoia_4.0_1280x960 (Green), Sequoia_4.0_1280x960 (Red), Sequoia_4.0_1280x960 (Red edge), Sequoia_4.0_1280x960 (NIR)
Rig name(s)	«Sequoia»
Average Ground Sampling Distance (GSD)	7.22 cm / 2.84 in
Area Covered	0.0941 km^2 / 9.4146 ha / 0.0364 sq. mi. / 23.276 acres

Quality Check

Images	median of 12298 keypoints per image	✓
Dataset	2172 out of 2180 images calibrated (99%), all images enabled	✓
Camera Optimization	0.04% relative difference between initial and optimized internal camera parameters	✓
Matching	median of 5592.89 matches per calibrated image	✓
Georeferencing	yes, 7 GCPs (7 3D), mean RMS error = 0.022 m	✓

Figure A.17: Pix4D Report for 50 and 70m multispectral flights

Summary   ⓘ

Project	MTE_MS_90M
Processed	2017-09-26 12:10:52
Camera Model Name(s)	Sequoia_4.0_1280x960 (Green), Sequoia_4.0_1280x960 (Red), Sequoia_4.0_1280x960 (Red edge), Sequoia_4.0_1280x960 (NIR)
Rig name(s)	«Sequoia»
Average Ground Sampling Distance (GSD)	9.41 cm / 3.7 in
Area Covered	0.1925 km^2 / 19.2486 ha / 0.0744 sq. mi. / 47.5891 acres
Time for Initial Processing (without report)	01h:48m:27s

Quality Check   ⓘ

ⓘ Images	median of 12214 keypoints per image	✓
ⓘ Dataset	2060 out of 2104 images calibrated (97%), all images enabled, 2 blocks	⚠
ⓘ Camera Optimization	0.03% relative difference between initial and optimized internal camera parameters	✓
ⓘ Matching	median of 5952.15 matches per calibrated image	✓
ⓘ Georeferencing	yes, 13 GCPs (13 3D), mean RMS error = 0.017 m	✓

Summary   ⓘ

Project	MTE_RGB_90M
Processed	2017-09-25 19:54:05
Camera Model Name(s)	FC300X_3.6_4000x3000 (RGB)
Average Ground Sampling Distance (GSD)	3.84 cm / 1.51 in
Area Covered	0.2029 km^2 / 20.2907 ha / 0.0784 sq. mi. / 50.1654 acres

Quality Check   ⓘ

ⓘ Images	median of 14834 keypoints per image	✓
ⓘ Dataset	420 out of 428 images calibrated (98%), all images enabled	✓
ⓘ Camera Optimization	2.75% relative difference between initial and optimized internal camera parameters	✓
ⓘ Matching	median of 6448.43 matches per calibrated image	✓
ⓘ Georeferencing	yes, 13 GCPs (13 3D), mean RMS error = 0.026 m	✓

Figure A.18: Pix4D Reports for 90m multispectral and RGB flights